NASA/TM–2006-213489

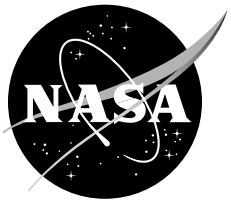

A Summary of the Experimental Results for a Generic Tractor-Trailer in the Ames Research Center 7- by 10-Foot and 12-Foot Wind Tunnels

Bruce L. Storms
AerospaceComputing, Inc.

Dale R. Satran, James T. Heineck, and Stephen M. Walker
Ames Research Center, Moffett Field, California

July 2006

The NASA STI Program Office . . . in Profile

Since its founding, NASA has been dedicated to the advancement of aeronautics and space science. The NASA Scientific and Technical Information (STI) Program Office plays a key part in helping NASA maintain this important role.

The NASA STI Program Office is operated by Langley Research Center, the Lead Center for NASA's scientific and technical information. The NASA STI Program Office provides access to the NASA STI Database, the largest collection of aeronautical and space science STI in the world. The Program Office is also NASA's institutional mechanism for disseminating the results of its research and development activities. These results are published by NASA in the NASA STI Report Series, which includes the following report types:

- TECHNICAL PUBLICATION. Reports of completed research or a major significant phase of research that present the results of NASA programs and include extensive data or theoretical analysis. Includes compilations of significant scientific and technical data and information deemed to be of continuing reference value. NASA's counterpart of peer-reviewed formal professional papers but has less stringent limitations on manuscript length and extent of graphic presentations.

- TECHNICAL MEMORANDUM. Scientific and technical findings that are preliminary or of specialized interest, e.g., quick release reports, working papers, and bibliographies that contain minimal annotation. Does not contain extensive analysis.

- CONTRACTOR REPORT. Scientific and technical findings by NASA-sponsored contractors and grantees.

- CONFERENCE PUBLICATION. Collected papers from scientific and technical conferences, symposia, seminars, or other meetings sponsored or cosponsored by NASA.

- SPECIAL PUBLICATION. Scientific, technical, or historical information from NASA programs, projects, and missions, often concerned with subjects having substantial public interest.

- TECHNICAL TRANSLATION. English-language translations of foreign scientific and technical material pertinent to NASA's mission.

Specialized services that complement the STI Program Office's diverse offerings include creating custom thesauri, building customized databases, organizing and publishing research results . . . even providing videos.

For more information about the NASA STI Program Office, see the following:

- Access the NASA STI Program Home Page at *http://www.sti.nasa.gov*

- E-mail your question via the Internet to help@sti.nasa.gov

- Fax your question to the NASA Access Help Desk at (301) 621-0134

- Telephone the NASA Access Help Desk at (301) 621-0390

- Write to:
  NASA Access Help Desk
  NASA Center for AeroSpace Information
  7121 Standard Drive
  Hanover, MD 21076-1320

NASA/TM–2006-213489

A Summary of the Experimental Results for a Generic Tractor-Trailer in the Ames Research Center 7- by 10-Foot and 12-Foot Wind Tunnels

Bruce L. Storms
AerospaceComputing, Inc.

Dale R. Satran, James T. Heineck, and Stephen M. Walker
Ames Research Center, Moffett Field, California

National Aeronautics and
Space Administration

Ames Research Center
Moffett Field, California 94035-1000

July 2006

Acknowledgments

This work was funded by the Department of Energy, Office of Heavy Vehicle Technology, under the direction of the late Dr. Sid Diamond. Significant input into the planning for this experiment came from the members of the Working Group on Heavy Vehicle Aerodynamic Drag headed by Rose McCallen of Lawrence Livermore National Laboratory.

Available from:

NASA Center for AeroSpace Information
7121 Standard Drive
Hanover, MD 21076-1320
(301) 621-0390

National Technical Information Service
5285 Port Royal Road
Springfield, VA 22161
(703) 487-4650

TABLE OF CONTENTS

NOMENCLATURE

A	=	tractor-trailer frontal area = w*h
C_D	=	body-axis drag coefficient = D / q*A
$\bar{C}_D$	=	wind-averaged drag coefficient
C_N	=	normal force coefficient
C_S	=	side force coefficient
C_{PM}	=	pitching moment coefficient
C_{YM}	=	yawing moment coefficient
C_{RM}	=	rolling moment coefficient
D	=	body-axis drag
g	=	distance from back of tractor to front of trailer
h	=	trailer height
l	=	base-flap length
L_P	=	sound-pressure level, dB
q	=	test-section dynamic pressure = $^1/_2\ \rho U^2$
Re	=	Reynolds number = U*w / ν
U	=	free-stream velocity
w	=	truck width
x	=	axial distance from front bumper
y	=	vertical distance from bottom of wheels
z	=	lateral distance from model centerline
ν	=	kinematic viscosity
ρ	=	air density
ψ	=	yaw angle (positive nose right)

A SUMMARY OF THE EXPERIMENTAL RESULTS FOR A GENERIC TRACTOR-TRAILER IN THE AMES RESEARCH CENTER 7- BY 10-FOOT AND 12-FOOT WIND TUNNELS

Bruce L. Storms

AerospaceComputing, Inc.

Dale R. Satran, James T. Heineck, and Stephen M. Walker

Ames Research Center

ABSTRACT

Experimental measurements of a generic tractor-trailer were obtained in two wind tunnels at Ames Research Center. After a preliminary study at atmospheric conditions in the Ames 7- by 10-Foot Wind Tunnel, additional testing was conducted at Reynolds numbers corresponding to full-scale highway speeds in the Ames 12-Foot Pressure Wind Tunnel. To facilitate computational modeling, the 1:8-scale geometry, designated the Generic Conventional Model, included a simplified under-body and omitted many small-scale details. The measurements included overall and component forces and moments, static and dynamic surface pressures, and three-component particle image velocimetry. This summary report highlights the effects of numerous drag reduction concepts and provides details of the model installation in both wind tunnels. To provide a basis for comparison, the wind-averaged drag coefficient was tabulated for all configurations tested. Relative to the baseline configuration representative of a modern class-8 tractor-trailer, the most effective concepts were the trailer base flaps and trailer belly box providing a drag-coefficient reduction of 0.0855 and 0.0494, respectively. Trailer side skirts were less effective yielding a drag reduction of 0.0260. The database of this experimental effort is publicly available for further analysis.

1.0 INTRODUCTION

For a typical heavy vehicle at a highway speed of 110 km/hr, the energy required to overcome aerodynamic drag is about 65% of the total expenditure (which includes rolling friction, transmission losses, and accessories). By altering the vehicle shape, it was estimated that modern truck aerodynamic drag coefficients may be reduced by up to 50%, resulting in an annual national fuel savings of eleven billion liters (ref. 1). This large potential savings coupled with increasing fuel costs has spurred renewed interest in heavy-vehicle aerodynamics.

A significant number of experimental studies of heavy-truck geometries were conducted in the 1970's and 1980's (ref. 2). The resulting first-generation drag-reduction technology currently in use includes cab shaping, cab-mounted deflectors, trailer front-end fairings, cab side extenders, and body front-edge rounding. The cab deflectors and side extenders accounted for the majority of the wind-averaged drag reduction reducing the pre-1980 drag level by about 25%. Other drag-reduction technologies that are not widely used include tractor-trailer gap seals, trailer side skirts, and rear boat-tailing. Each of these technologies produced a reduction of the wind-averaged drag coefficient between 0.03 and 0.10—which was about one-half the benefit of the first-generation technologies. However, the benefits of these devices are additive and the resulting net reduction was relatively large.

The aerodynamic drag reduction and fuel savings of various tractor and trailer modifications was previously summarized in reference 3. Since fuel consumption is the quantity of interest for commercial operators, a derivation of fuel consumption as a function of drag coefficient and road speed was provided. For trailer base flaps and skirts, the ranges of wind-averaged drag reduction were listed as 0.03–0.09 and 0.04–0.07, respectively.

More recently, a series of experimental and computational studies was funded by the Department of Energy (DOE), Office of Heavy Vehicle Technology. With the goal of CFD validation, the experimental efforts have focused on simplified geometries at 1:8-scale and below. Early experiments (refs. 4–6) focused on the simplified geometry of the Ground Transportation System (GTS) model representative of a class-8 tractor-trailer with a cab-over-engine design. The 1:8-scale GTS model with no tractor-trailer gap and no wheels was first studied with the addition of several ogival boattails and slants to the base of the trailer (ref. 4). The largest overall drag reduction of 10% was obtained by a 2.4 m ogive configuration (full scale). The addition of boattail plates to the same model resulted in a 19% drag reduction, and PIV measurements behind the trailer document a significant reduction in the wake size due to the flow turning provided by the plates (ref. 5). Variation of the tractor-trailer gap on a 1:15-scale model at zero yaw revealed relatively constant drag on the tractor while the trailer drag increased by a factor of three as the gap was increased from zero to $1.55*A^{0.5}$ (ref. 6).

Also part of the DOE effort, a 1:8-scale generic tractor-trailer geometry was developed with numerous simplifications to facilitate CFD validation efforts. This geometry, known as the Generic Conventional Model (GCM) was the focus of the current report. The GCM includes a simplified tractor geometry, a variable tractor-trailer gap, and a trailer with a simplified underbody. The GCM was tested in two facilities at Ames Research Center: 1) the 7- by 10-Foot Wind Tunnel (an

atmospheric facility), and 2) the 12-Foot Pressure Wind Tunnel (capable of total pressures up to 6 atmospheres). The goal of this report was to document the two experimental efforts with details of model installation, instrumentation, and differences between the two wind tunnels. Because of the size of the experimental data sets, only limited results were provided to highlight specific configurations and explain differing results. A summary of all configurations is included to facilitate the use of the publicly available data set for CFD validation.

2.0 EXPERIMENTAL SETUP

Measurements of the same model were obtained in both the 12-Foot Pressure Wind Tunnel and the 7- by 10-Foot Wind Tunnel at Ames Research Center. Details of the model, wind tunnels, and installations are provided below.

2.1 Generic Conventional Model

A photograph of the GCM installed in the 12-Foot Wind Tunnel test section is shown in figure 1. This 1:8-scale model was representative of a generic class-8 tractor-trailer with the engine in front of the cab. Designed for CFD validation, the model included a number of geometry simplifications in order to facilitate grid generation and avoid the associated flow complexities. In particular, no effort was made to duplicate the complex geometry of the undercarriage of either the tractor or trailer (both were approximated by flat surfaces). Similarly, the wheel wells of the tractor were not modeled and only the portions of the wheels below the tractor lower surface were included (fig. 2). Also, the tractor geometry (designed by the Calmar Research Corp.) was a streamlined shape representative of a modern tractor design that omitted most small-scale surface details and flow-through components. The trailer measured 13.7 m in length (full scale) with rounded front vertical edges (20-cm full-scale radius). The tractor-trailer gap for this study was held constant at the full-scale equivalent of 1 m. The moment center on the model was specified as the point between the rear tractor wheels along the model centerline at the bottom of the wheels.

In both tunnels, the tractor was suspended from the trailer through a set of flexures and 2 load cells that measured the drag and yawing moment of the tractor alone. The specified accuracy of the load cells was ±2 N. The model was instrumented with 200 pressure taps on the tractor and 276 taps on the trailer. The relative locations of these pressure taps on the tractor and trailer are shown in figures 3 and 4, respectively. The surface pressures were acquired at a sample rate of 24 Hz with an electronically scanned pressure system. There were also 12 dynamic pressure transducers mounted on the tractor rear surface, trailer front surface, and the trailer rear surface as shown in figure 5. The dynamic pressures were sampled at 1500 Hz and 2560 Hz in the 7- by 10-Foot and 12-Foot Wind Tunnels, respectively. The sample duration of the above measurements varied with the instrumentation configuration. The data acquisition parameters as well as the locations of both the static pressure taps and the dynamic pressure transducers are tabulated in the data set.

A three-component PIV system was used to obtain horizontal-plane velocity measurements in the tractor-trailer gap (7x10 and 12-Foot) and in the trailer wake (7x10 only) at 1/4, 1/2, and 3/4 of the

trailer height. The data set includes both instantaneous and averaged data for each location. All measurements were acquired for Mach and Reynolds numbers of 0.15 and 1.1 million, respectively. In addition, PIV data were obtained at M = 0.15 and Re = 4.8 million in the 12-Foot Pressure Wind Tunnel. Measurements at higher Reynolds numbers were not possible due to pressure-related limitations of the PIV instrumentation. Details of the PIV system installation are presented in references 7–8.

2.2 Ames 7- by 10-Foot Wind Tunnel

The Ames 7- by 10-Foot Wind Tunnel is a closed-circuit atmospheric facility incorporating a 4.57 m long test section with a constant height of 2.13 m and a nominal width of 3.05 m with a 1% wall divergence. The boundary layer thickness at the test section entrance is 5.3 cm, which corresponds to a displacement thickness of 1.5 cm. The multiple turbulence-reducing screens in the circuit yield empty test-section turbulence intensities in the longitudinal, lateral, and vertical directions of 0.1%, 0.3%, and 0.3%, respectively, for a test condition of M = 0.22. These turbulence levels correspond to a RMS turbulence intensity of 0.25% and a turbulence factor of 1.2. Forty-three static pressure taps were located on the right tunnel wall (looking upstream) in one vertical and two horizontal rows, as shown in figure 6. For ease of comparison with CFD, the test section static pressure was obtained from a single wall pressure tap located at x/w = 4.5, y/w = 2.6, and z/w = –4.7. Except where noted, all data were acquired at a Mach number of 0.15 and a Reynolds number of 1.1 million.

In the 7- by 10-Foot Wind Tunnel, the model was located at a position 13.33 cm downstream of the beginning of the test section. Mounted level in the test section, the bottoms of the wheels were located 1.5 cm above the wind tunnel floor to account for the boundary-layer displacement thickness. Due to the cantilevered mounting of the tractor, the front wheels were only 9 mm above the floor (this inclination is evident in the “as-built” geometry definition included with the data set). Four cylindrical struts connected the model to the scale system and 3.8-cm diameter cylindrical fairings (non-metric) extended from the floor to within 0.63 cm of the bottom of the model. The model was mounted on the facility scale system that included a turntable for remote model positioning. The center of rotation of the model was located 1.32 m aft of the tractor front bumper, and the model was yawed through a range of angles between ±14 degrees. Since the facility scales measure wind-axis forces (parallel and perpendicular to the axis of the wind tunnel), a coordinate transformation was employed to determine the body-axis drag (the force along the longitudinal axis of the model). The model frontal area of 0.154 m^2 gave a solid blockage of 2.4%.

2.3 Ames 12-Foot Pressure Wind Tunnel

The Ames 12-Foot Pressure Wind Tunnel can be pressurized from 0.25 to 6 atmospheres at Mach numbers from 0.1 to 0.5. The test section has a nominally circular cross section 3.66 m in diameter with four 1.22 m wide flat surfaces centered about the horizontal and vertical centerlines. The RMS turbulence intensity in the test section was 0.27% and 0.52% at Reynolds numbers of 1 and 6 million, respectively. A ground plane was installed 53 cm above the tunnel floor providing a flat surface 3.05 m wide and 5.49 m long (a typical installation is shown in figure 7). Pressure taps were located on both the test-section walls (8 rows of 30 taps, fig. 8) and the ground plane (2 rows of 64

taps, fig. 9). A fairing was installed below the ground plane to isolate the model-support hardware from the air stream, and speed-correction probes were used to correct the facility speed due to the blockage of the ground plane and fairing. There was also an additional pitot-static probe installed on the upper left ceiling to measure the free-stream conditions in the test section. All of the data presented were referenced to the Mach number based on a wall tap located 1.88 m forward of the center of rotation at an azimuth of 60 deg from vertical (two o'clock looking downstream). Except where noted, all data were acquired at a Mach number of 0.15, which allowed for Reynolds number studies with no Mach-number effects. With the tunnel pressurized to six atmospheres, the Reynolds number was over 6 million based on the trailer width, which was comparable to a full-scale truck driving at 120 km/hr.

In the 12-Foot Wind Tunnel, the GCM was attached to the model-support hardware with four vertical posts. Measuring 4.45 cm in diameter, the four posts formed a square 19.68 cm on a side with the two aft posts 0.98 m forward of the trailer end. The posts were non-metric (i.e., their aero loads were not measured by the balance) with 0.75 mm of clearance as they passed through the trailer floor. The model was mounted with its wheels 3.8 mm above the ground plane (with the tractor nominally level) and centered laterally in the tunnel. The center of rotation of the model was located 1.38 m aft of the tractor front bumper and 2.74 m aft of the ground plane leading edge. Based on the model frontal area, the solid blockage of the GCM in the 12-Foot Wind Tunnel was 1.5%. The overall model loads were measured with a six-component balance (10 cm Task balance Mark 2B) that was mounted inside the trailer. The manufacturer-specified accuracy of the internal balance in the axial (drag) direction was ±4.45 N, but the experimental data indicated repeatability on the order of ±2.2 N. The uncertainties in the force, moment, and pressure coefficients are summarized in Table 1 for both wind tunnels. These uncertainty bands include both measurement resolution and point-to-point repeatability.

TABLE 1. FORCE, MOMENT, AND PRESSURE COEFFICIENT UNCERTAINTY (±).

Tunnel Rex10^6	C_L	C_D	C_S	C_{PM}	C_{YM}	C_{RM}	C_P
12-Ft (6.2)	0.043	0.002	0.021	0.040	0.020	0.006	0.002
12-Ft (1.1)	0.250	0.009	0.125	0.236	0.118	0.035	0.010
7x10 (1.1)	0.075	0.009	0.036	0.200	0.034	0.500	0.004

3.0 RESULTS AND DISCUSSION

The model configurations tested in both tunnels are listed with the corresponding test conditions in Appendix A. Unless otherwise specified, all measurements were conducted at a Mach number of 0.15. The Reynolds numbers listed are nominal (more precise values are available in the publicly available data set). Note that the "best extenders" configuration differed for the two facilities due to the increased effectiveness of the longer cab extenders at higher Reynolds number (detailed below).

The optimum extender lengths in the 7- by 10-Foot and 12-Foot Wind Tunnels was 50% and 60% of the tractor-trailer gap, respectively. As a result, a direct comparison was not possible between the results from the two wind tunnels for configurations including "best extenders" (configurations 13 & 18, in particular).

3.1 Choice of Baseline for CFD Comparison

As reported previously in reference 9, the no-extender GCM configuration exhibited significant hysteresis and a rapid rise in drag near zero yaw. In a separate study, a more realistic 1:10-scale geometry with a standard aero package and side extenders (fig. 10) was investigated experimentally at Canada's National Research Council (NRC) Institute for Aerospace Research (ref. 10). The comparison of experimental results highlighted the atypical drag curve of the GCM geometry (fig. 11). Due to the numerous geometry simplifications, the drag of the GCM geometry was expected to be lower than that of a higher-fidelity model. However, the rapid rise in drag exhibited by the GCM model was atypical of more realistic geometries and served to exaggerate the effectiveness of the cab extenders. This rapid drag rise was likely due to the effect of the simplified tractor geometry on the tractor-trailer gap flow. Since the addition of the side and roof extenders resulted in a more representative drag curve, it is recommended that the best extender configuration (config. 8) be used as a baseline for comparison. The Reynolds number sensitivity of wind averaged drag for this configuration was previously presented in reference 9.

3.2 Wind-Average Drag

Using the variation of drag with yaw angle, wind-averaged drag coefficients ($\overline{C}_D$) were computed using the SAE Recommended Practice (ref. 11). This practice assumed that the mean wind speed in the United States of 11.2 km/hr has an equal probability of approaching the vehicle from any direction. This mean wind speed and the vehicle velocity were used to calculate a weighted average based on the variation in drag coefficient over a range of yaw angles. The wind-averaged drag coefficients reported in this paper were computed for a highway speed of 88 km/hr. Note that the uncertainty in the wind-averaged drag coefficient was less than the values listed in table 1 due to the effects of averaging. In particular, the repeatability of the wind-averaged drag for the baseline with best extenders (config. 8) was ±0.001 and ±0.005 in the 12-Foot and 7- by 10-Foot Wind Tunnels, respectively.

A summary of the wind-averaged drag coefficients is tabulated by configuration in appendix B for Reynolds numbers of 1.1 and 6.2 million. Also included is the difference in wind-averaged drag coefficient ($\Delta\overline{C}_D$) relative to the best extender baseline (config. 8). Note that a negative $\Delta\overline{C}_D$ corresponds to a drag reduction. The discussion below provides an overview of the configurations tested and addresses the discrepancies between data sets.

3.3 Tractor-Trailer Gap

The tractor-trailer gap was of greatest concern when there was significant cross wind that resulted in crossflow through the gap. Several add-on devices were tested on the tractor, including side and roof extenders, a cab extender, and a gap filler (fig. 12). Similar to the components of a modern tractor aero package, side and roof extenders were attached to the rear of the tractor as shown in figure 12(b). The extenders were 1/8-in. thick (model scale) with four different lengths ranging from 30% to 60% of the tractor-trailer gap. As discussed above, the most effective side and roof extender length of 60% gap was chosen as the baseline for all subsequent comparisons in the current analysis. The wind-averaged drag of this configuration was 0.422. The cab splitter (fig. 12(c)) consisted of a flat plate 60% of the tractor-trailer gap in length that was mounted to the back of the tractor at the model centerline. The gap filler (fig. 12(d)) was a smooth transition from the tractor to the trailer with no gap at all. Although impractical from an operational perspective, this configuration was included to measure the effect of a full-gap fairing and provide a basis for comparison with previous simple geometries.

The comparison of drag and yawing-moment coefficients for these add-ons (fig. 13) revealed marginal differences near zero yaw and significant variations for higher cross winds. The cab splitter significantly reduced the drag for yaw angles greater than ±2 deg when added to the no-extender configuration. The wind-averaged drag of the cab splitter, however, was significantly greater ($\Delta \bar{C}_D = 0.0501$) than that of the side- and roof-extender baseline. The drag curves of the gap filler and extender baseline were very similar, except at the higher yaw angles, where the gap filler provided slightly greater drag reduction. The calculation of wind-averaged drag yielded a slight drag increase ($\Delta \bar{C}_D = 0.0005$) relative to the extender baseline, but the difference was within the observed repeatability in the 7- by 10-Foot Wind Tunnel. Except for the no-extender case, the yawing-moment coefficient curves were similar for low yaw angles, with significant differences only for yaw angles above 6 deg.

Since tractor aero packages typically only include side extenders, the effect of the roof extender was investigated by testing the side extenders alone in the 7- by 10-Foot Wind Tunnel. The drag curves (fig. 14) indicated that the addition of a roof extender provided a significant drag reduction at all yaw angles. The change in wind-averaged drag for side extenders only relative to the baseline was 0.009. The effect of the roof extender on the yawing moment (not shown) was minimal with minor differences evident at the higher yaw angles. A more detailed analysis of this configuration was previously presented in reference 12.

The wind-averaged drag reduction provided by the extenders was plotted as a function of extender length in figure 15. For the four extender lengths tested between 30% and 60% gap width, there was a consistent trend of increasing drag reduction with increasing extender length. More specifically, the drag reduction increased from 0.145 to over 0.155 for an increase in extender length from 30% gap to 60% gap. As previously discussed, the drag reduction of the side and roof extenders was exaggerated due to the uncharacteristic drag curve of the no-extender GCM configuration. Although these data suggest that additional drag reduction may be obtained from longer extenders, the gap filler (as detailed above) yielded only marginal differences by completely blocking the gap crossflow.

To determine the effect of Reynolds number, the facility total pressure was varied while the Mach number was held constant in the 12-Foot Pressure Wind Tunnel. The change in wind-averaged drag coefficient with Reynolds number (fig. 16(a)) revealed differing sensitivities for the GCM with and without side and roof extenders. In figure 16(a), the error bars on the no-extender data points show the magnitude of experimental uncertainty due to both measurement resolution and repeatability. Error bars were of the same magnitude for the extender configuration, but were omitted from the figure for clarity. For the no-extender case, the drag coefficient was observed to increase by an average of 0.006 for Reynolds numbers less than 4 million. The extender configuration, however, did not indicate a significant increase until below 3 million with a dramatic increase, close to 0.03, at Re = 500,000. The drag curves for the extender configuration at several Reynolds numbers (fig. 16(b)) illustrated a significant increase in drag that increased with yaw angle at Re = 500,000. This was likely due to flow variations in the vicinity of the trailer leading-edge curvature which was more sensitive to Reynolds number than sharp corners.

The GCM was instrumented with 476 surface pressure taps, some of which were located on the back of the tractor (39) and the front and back of the trailer (24 and 39, respectively). Figures 17–19 present pressure coefficient contours on these surfaces for the baseline configuration at yaw angles of zero and 10 deg. Note that all but three pressure taps were located on the left side of the model with clustering near the edges. For zero yaw, symmetry was assumed and the data were duplicated on the right side of the figure. For 10 deg, the right half of the figure included data for the –10 deg yaw angle.

In both test facilities, particle image velocimetry (PIV) measurements were obtained in the gap between the tractor and trailer at yaw angles of zero and 10 deg. The 12-Foot Wind Tunnel results were previously reported for a configuration without side extenders (ref. 9). In the 7- by 10-Foot Wind Tunnel, measurements were conducted with and without 50%-gap side extenders and the resulting stream traces (fig. 20) indicated their effect on the gap flow. At zero deg, the flow fields with and without extenders were similar with two counter-rotating recirculation regions. Closer examination revealed that the presence of the extenders tended to move centers of these regions closer to the cab, minimizing crossflow, and reducing the vertical velocity (Vmean) in the gap. At 10 deg, the stream traces without extenders indicated one recirculation region to the right with dramatic crossflow and downflow. The effect of the extenders was to reduce both crossflow and downflow (thereby increasing pressure), which resulted in a low-vorticity recirculation near the middle of the gap. A more detailed discussion of the PIV measurements is found in reference 7.

In addition to PIV, eight dynamic pressure sensors were located in the gap region to quantify the fluctuating pressure field. The effects of the 60%-gap tractor side and roof extenders on the auto-spectra of the mid-height left-hand sensors are shown in figure 21 for yaw angles of zero and 10 deg. At a yaw angle of 10 deg, the extenders significantly reduced the dynamic pressure level by approximately 10–20 dB relative to the no-extender case (except for frequencies above 400 Hz on the trailer). At zero yaw, there was a smaller reduction of 3–10 dB at most frequencies. On the rear of the tractor (fig. 21(a)), the best-extender spectra for both angles were very similar, while those of the no-extender case were significantly different. Without extenders, there was a significant spectral peak at about 400 Hz for zero yaw, which was notably absent at 10 deg. In contrast, the 10-deg no-extender spectra contained two low frequency peaks near 40 and 120 Hz. With extenders, there was significant spectral content spread between 300 and 400 Hz, most visible on the tractor rear. On the

front of the trailer (fig. 21(b)), the spectrum for the best-extenders case at 10-deg indicated significantly elevated levels at frequencies above 100 Hz relative to that of zero yaw. The sharp spectral peaks at 60 and 120 Hz were due to the AC power supply and should be ignored in all spectra.

Figures 22–23 illustrate the effect of yaw angle and sensor position on the dynamic pressure spectra on the tractor rear and trailer front with side and roof extenders. On the tractor rear at zero yaw (fig. 22(a)), the spectra from the mid-height sensors were very similar while that of the upper sensor contained a notable peak around 700 Hz—possibly a harmonic of the lower-frequency content at 300–400 Hz. This peak was also evident at 10 deg where the spectrum of the leeward sensor (on the right) was significantly higher than the others. In contrast to those of the tractor rear, the spectra from the sensors on the front of the trailer were relatively devoid of spectral peaks, but varied in level with the lowest level from the bottom sensor. At 10 deg, the levels were significantly higher for all but the right (leeward) sensor, which actually decreased relative to that of zero yaw.

In addition to the auto-spectra, the coherence between sensors was also computed. The signal coherence between two sensors was calculated as the square of the cross-correlation divided by the individual auto-correlations, which can be expressed as:

$$C_{xy}(\omega) = | P_{xy}(\omega) |^2 / (P_{xx}(\omega) * P_{yy}(\omega))$$

This quotient results in a real number between 0 and 1 that is a measure of the correlation between two signals x(n) and y(n) at a frequency ω. A coherence of 1 indicated perfect correlation (i.e., identical signals) while a value of zero indicated no signal correlation. As with the auto-spectra, sharp peaks at 60 and 120 Hz were the result of AC power and should be ignored in all of the coherence spectra that follow.

The coherence between neighboring sensors on the back of the tractor is presented in figure 24 for yaw angles of zero and 10 deg. Since sensor #3 was inoperable, no coherence results are shown for any combination with that sensor. In addition, coherence was also shown for the left mid-height sensor (#2) and the corresponding sensor on the trailer (#6). At zero yaw, there was strong coherence between all sensors on the tractor at about 400 Hz. This peak corresponded to the peak in the auto-spectra observed above. At 10 deg, however, this peak was replaced by lower-frequency content at 40–45 Hz. There also appeared to be a significant peak near 120 Hz for the 2:6 coherence that did not fit the characteristic of the sharper electronic-noise coherence. These significant differences in auto-spectra and coherence noted between zero and 10 deg were most certainly due to the vastly different flow patterns measured for these conditions with PIV (detailed above).

The effect of the side and roof extenders on the coherence between neighboring sensors on the tractor rear is presented in figure 25 for yaw angles of zero and 10 deg. In contrast to the 400-Hz peak noted above for the no-extender configuration, there was a broad peak of high coherence at 200–500 Hz. Marginally lower, a second broad peak centered around 750 Hz (possibly a harmonic of the first) was most pronounced in the 1:2 coherence at both yaw angles. Unlike the results for the no-extender case, the coherence spectra of the extender configuration were generally similar for zero and 10 deg.

The coherence between neighboring sensors on the front of the trailer with and without extenders is presented in figures 26–27. These plots present coherence only up to 500 Hz since no significant coherence was observed at higher frequencies. The coherence on the front of the trailer without extenders was similar to that of the tractor rear, but at significantly reduced levels. With extenders, however, the observed coherence at 300–400 Hz was present, but at minimal levels.

The coherence between sensors on the tractor rear and sensors on the trailer front are detailed in figures 28–30. Similar to the coherence for the tractor sensors noted above, all tractor-trailer coherence spectra included some level of coherence at 300–400 Hz. There was also signal coherence for frequencies above 600 Hz for selected sensor combinations, but only at zero yaw. In particular, signal coherence of about 0.6 was evident at about 750 Hz for sensor combinations of 1:7 and 4:7, a possible result of the down flow measured with PIV. At 10 deg, all coherence levels were significantly reduced, except for those including sensor #8 as a result of the crossflow through the gap. In addition, the 10-deg correlations also indicated significant coherence at about 10 Hz. The source of this low frequency coherence could have been related to a vibrational mode of the model.

Both the auto-spectra and spectral coherence for sensors in the tractor-trailer gap indicated significant correlations in the 300–400 Hz range and higher frequencies for some configurations. For a sharp-edged bluff body such as the GCM geometry, Strouhal shedding was a likely source of flow unsteadiness. Typical Strouhal numbers for bluff bodies range from 0.14 to 0.16 (ref. 13), which correspond to a frequency range of 22–25 Hz (based on model width). The absence of spectral peaks in this range suggested that, in the presence of the trailer, the separated flow field was dominated by the vortex system in the tractor-trailer gap. In this case, the source of the high frequency dynamic content (> 200 Hz) was likely due to a combination of shear-layer shedding instabilities and oscillatory modes of the vortex structures identified by PIV. These results suggested that time-accurate simulations of this flow field should contain sufficient resolution to compute frequencies up to at least 500 Hz.

3.4 Trailer Base

Estimated to be the largest source of tractor-trailer drag, the rear of the trailer can yield significant drag reduction by way of devices that promote base-pressure recovery. In this experimental effort, the devices tested were base flaps, boattail plates, and vortex generators. Each device is addressed in detail below.

Base Flaps. As previously documented (ref. 3), base flaps were an effective method of aerodynamic boat-tailing. In this study, the panels were attached to all edges of the trailer base and angled inward. Measurements were made for a base-flap length of 63.5 cm full scale (non-dimensional length $= l / A^{0.5} = 0.20$) at angles ranging from zero to 28 deg. The installation photos (fig. 31) show the base flaps with 8- and 20-deg deflections mounted on the rear of the trailer. Note that the linkages connecting the flaps to the base were designed for easy angle change and are not representative of the full-scale hardware.

The effect of the base flaps on the drag and yawing-moment coefficients is presented in figure 32 for a flap angles from 8 to 20 deg. Relative to the side and roof extenders alone, the addition of the base

flaps generally provided significant drag reduction that marginally increased with yaw angle. Greater reductions in drag were observed at higher flap angles, with the largest increment occurring between 12 and 16 deg. Diminishing returns in drag reduction were obtained in increasing the flap angles to 20 deg (optimum for this configuration). The effect of base flaps on the yawing moment coefficient was a general increase in the absolute value with increasing flap angle. By comparing the change of component drag and yawing moment coefficients (fig. 33), it was evident that the trailer alone was the source of the observed differences.

The effect of base-flap angle on wind-averaged drag reduction is presented in figure 34. Different symbols were used to indicate the data from two separate wind-tunnel entries (four months apart) of the same model in the Ames Research Center 12-Foot Pressure Wind Tunnel. The lower Reynolds number on the second entry was due to limitations of the coincident PIV measurements. Although there was an unexplained offset in the two curves (addressed in a subsequent section), the trends indicated that the optimum base-flap angle was around 20 deg. The wind-averaged drag coefficient with 20-deg base flaps was 0.3360, which was 0.0954 less than the side- and roof-extender baseline (2nd entry, run 242). Previous small-scale experiments (ref. 3) and full-scale road tests (ref. 14) (both without the lower base flap) yielded an optimum base-flap angle closer to 15 deg. Since the Reynolds-number effects for the base flaps were observed to be minimal, the higher optimum angle of the current study may be attributed to the presence of the lower base flap, differences in flap length, and/or differences in geometry.

The trailer was instrumented with a line of pressure taps running axially along the centerline of the top and left side. The pressure distributions with and without base flaps are presented in figures 35–36 for yaw angles of zero and 10 deg. On both the top and side, the base flaps served to reduce the pressure towards the rear of the trailer. The effect of the base flaps on the forward two-thirds of the pressure distribution was minimal. The pressures on the tractor (not shown) were unaffected. Hence, the base flaps had a relatively local effect on the truck pressure distributions. The pressure distributions at –10 deg (not shown) exhibited similar trends.

The differences in the pressure distributions on the back of the trailer with base flaps (fig. 37) indicated significantly increased pressures relative to the baseline. At zero yaw, the increase in pressure was relatively constant with an average change in pressure coefficient of 0.14. At 10 deg, however, the increase in pressure was far from uniform with the greatest increase on the bottom half of the trailer base. The extremes of the pressure difference occured on the windward side of the trailer base. The pressures on the back of the tractor and front of the trailer (not shown) were relatively unchanged by the presence of the base flaps.

In addition to the static pressure measurements, dynamic pressure sensors provided details of the fluctuating pressure field on the trailer. The auto-spectra on the trailer with and without 16-deg base flaps are shown in figure 38 for the mid-height sensor at yaw angles of zero and 10 deg. As expected, there was little effect of the base flaps on the dynamic pressures on the front of the trailer. On the rear of the trailer, however, the base flaps resulted in reduced dynamic pressure levels for both zero and 10 deg yaw. Apart from the peaks due to the power supply (at 60 Hz and its harmonics), there was also a lower frequency peak around 20–25 Hz that was most evident for the no-flaps case at 10 deg. A comparison of all four sensors on the trailer rear (fig. 39) revealed increasing levels with sensor height for low frequencies (<100 Hz) and the opposite trend at higher

frequencies. Since the resulting spectral coherence showed very low levels at the higher frequencies, the plots of figure 40 detail the coherence only up to 50 Hz. At zero yaw, there was significant spectral coherence for most sensor pairs at 22 Hz. This peak corresponded to a Strouhal number of 0.14, which was within the expected range for sharp-edged bluff-body geometries. At 10 deg, the coherence of the Strouhal shedding was reduced and there was also evidence of significant spectra coherence below 10 Hz. As previously discussed, this low-frequency content was likely related to a vibrational mode of the model.

Boattail Plates. Aerodynamic boat-tailing devices have several different variations, but boattail plates typically refer to panels mounted perpendicular to the trailer base and inset from the edges of the trailer. In this case, the same boattail plates that were studied on the simplified GTS model (ref. 5) were applied to the rear of the GCM trailer, as shown in figure 41(a). The plates extended 9.52 cm from the end of the trailer and were inset from the sides and top of the trailer by 1.6 cm. The bottom plate was mounted flush with the bottom of the trailer. In addition to this configuration, boattail plates with a length of 7.62 cm were also tested with and without a 1.6 cm fillet as shown in figure 41(b). A "scalloped" boattail plate configuration (fig. 41(c)) was also investigated with a nominal length of 8.57 cm that tapered down to 5 cm in the corners and included a 2.5 cm bottom plate flush with the bottom of the trailer. In contrast to the boattail plates, the rounded base plate (fig. 41(d)) was a 1.8 cm thick plate covering the entire trailer base with a 1.8-cm radius on the vertical and top horizontal edges.

Relative to the side and roof extenders only, all of the boattail plates significantly reduced the drag by a relatively constant margin for the entire yaw range (fig. 42(a)). Except for the rounded base plate, all boattail configurations provided similar levels of drag reduction with $\Delta \overline{C}_D$ ranging from –0.0512 to –0.0582. The original (standard) boattail-plate configuration proved to be the most effective, but significantly less effective than the optimum base-flap configuration ($\Delta \overline{C}_D = -0.0954$). The addition of the fillets to the shortened boattail plates ($\Delta \overline{C}_D = -0.0512$) provided an additional drag reduction of 0.0062 resulting in $\Delta \overline{C}_D = -0.0573$, only 0.0009 less than the standard boattail plate configuration. Generally speaking, all boattail plates generated greater yawing-moment magnitudes for non-zero yaw angles with the greatest differences at the higher angles (fig. 42(b)).

PIV measurements of the truck wake were conducted in the 7- by 10-Foot Wind Tunnel with and without the standard boattail plates at a Reynolds number of 1 million. The PIV images with and without boattail plates (fig. 43) illustrate how aerodynamic boat-tailing served to reduce the wake size by deflecting the flow inward. The reduced wake size of the boattail configuration resulted in the increased base pressures and reduced overall drag documented above. The data set included PIV measurement in the trailer wake at 1/4, 1/2, and 3/4 of the trailer height. No PIV data were obtained from the truck wake in the 12-Foot Wind Tunnel due to technical difficulties encountered in the high-pressure environment.

Vortex Generators. With the hope of reducing the truck wake size by adding vorticity (and thereby increasing the base pressure), vortex generators were attached to the trailer side in two rows at the middle and end of the trailer, respectively (fig. 44). At a Reynolds number of 1 million in the 7- by 10-Foot Wind Tunnel the resulting drag curves (fig. 45) show that all of the configurations tested increased the measured drag relative to the extender-only baseline. The drag increase was exacerbated at higher yaw angles, especially for the two configurations with mid-trailer vortex

generators. Relative to the baseline, the yawing moment was marginally reduced for all vortex-generator configurations.

3.5 Trailer Underbody

Several drag-reduction concepts were studied with the goal of reducing the lateral flow under the trailer. The trailer belly box (fig. 46(b)), so named because of its resemblance to the design of moving trailers, formed an enclosed box that extended from just aft of the tractor to the end of the trailer with openings in the bottom for the rear wheels. Trailer skirts have been previously investigated (ref. 3) as an effective add-on to minimize the crossflow under the trailer and shield the rear wheels. As shown in figure 46(c), the side skirts extended from a short distance behind the tractor to just in front of the rear wheels. The full-skirt configuration (fig. 46(d)) extended to the rear of the trailer covering the trailer wheels and also included lateral panels at the trailer base and behind the tractor bed. As the name implies, the centerline splitter (fig. 46(e)) was a single plate attached to the trailer centerline extending from the rear of the tractor to the front of the trailer wheels. Lastly, the cross splitter (fig. 46(f)) was a plate mounted laterally just behind the tractor rear wheels. All of these configurations measured 0.355 truck widths in height allowing a full-scale ground clearance of 0.3 m.

Belly Box and Skirts. The varying effects of the trailer belly box and skirts on the drag and yawing-moment coefficients are presented in figure 47 for Re = 6.3 million. Relative to the extender-only case, the trailer belly box was the most effective ($\Delta \bar{C}_D = -0.0494$). By far a more practical device, the side skirts were significantly less effective ($\Delta \bar{C}_D = -0.0359$) while the full-skirt configuration increased the wind-averaged drag ($\Delta \bar{C}_D = 0.0068$). The increase in drag of the full-skirt configuration was likely due to the cavity flow that forms inside the skirt. The trailer side skirts had a minimal effect on the yawing moment while the full skirts and belly box provided a reduction of the yawing moment magnitude for non-zero yaw angles. Since the trailer side skirts were the most practical and promising drag reduction concept, additional details of this configuration are provided below.

The effects of the side skirts on the component drag and yawing-moment differences are presented in figure 48. Similar to that of the base flaps, the change in drag coefficient by component indicated that the measured drag reduction was due to the effect of the skirts on the trailer. However, the skirts also generated a smaller, but measurable drag increase on the tractor. The total difference in yawing moment for the skirts was approximately half of that generated by the base flaps. Unlike the base flaps, both the tractor and trailer contributed to the observed yawing-moment differences.

The axial pressure distributions on the side and bottom of the trailer (figs. 49–50) illustrate that the general effect of the skirts was to reduce the pressures, especially on the bottom at ±10 deg. As suggested previously, the reduced pressures on the bottom of the trailer accounted for the reduced normal force generated by the skirts. Especially at high yaw angles, the windward skirt likely generated significant vorticity from the accelerated flow separating off the lower edge. The axial pressures on the side indicated slightly higher pressures on the forward third of the trailer except at –10 deg where the taps were on the leeward side. At mid-length on the side of the trailer, the skirts

provided a noticeable decrease in pressure. The pressure distribution on the top of the truck (not shown) was relatively unchanged.

The contour plots of figures 51–53 show the effect of the trailer skirts on the pressure distributions on the back of the tractor and the front and back of the trailer. At zero yaw, there appeared to be little difference on all three surfaces except for a slight increase in pressure on the back of the trailer. At 10 deg, a significantly larger increase in pressure was evident on the back of the trailer, especially on the right (leeward) side. A lesser increase in pressure was also observed on the front of the trailer, mainly on the upper half. A small decrease in pressure was also discernable on the back of the tractor, which accounted for the observed increase in tractor drag.

Splitters. As shown in figure 54, the centerline splitter provided a relatively small drag reduction ($\Delta \bar{C}_D = -0.0044$) while the cross splitter resulted in a large drag increase ($\Delta \bar{C}_D = +0.0356$). Similar to the trailer skirts, the centerline splitter served to reduce the cross flow under the truck. However, the resulting drag reduction was significantly less than that of the side skirts, since the trailer wheels and associated underbody structure were not completely shielded. In contrast, the cross splitter blocked streamwise flow along the underbody of the tractor resulting in an increase in drag at all yaw angles. With significant cross flow, this effect was exacerbated. The effect of the centerline splitter on yawing moment was minimal except at high yaw angles while the cross splitter served to reduce the yawing moment relative to the extender baseline.

3.6 Simplified Configurations

For comparison with the GTS data (ref. 5), a simplified configuration was tested with a filled tractor-trailer gap, the belly box installed, and the wheels removed (fig. 55). Along with the 60%-extender baseline, the drag curves for the GTS and simplified GCM are shown in figure 56a for a Reynolds number of 1 million. Due to instrumentation issues, drag coefficients for the GTS model are presented for positive yaw angles only. All of the simplified configurations generated significantly less drag than the best extender baseline, illustrating the combined effect of the tractor-trailer gap and the simplified underbody components. Relative to the GCM curves, the GTS drag curve was significantly lower due to its simplified geometry. The yawing-moment coefficient curves (fig. 56(b)) indicated significantly lower yawing moments for the simplified GCM configuration. In contrast, the yawing moment of the GTS model about the same relative location was similar to that of the best extender configuration, except at high yaw angles where it did not drop off. This is likely due to the more forward location of the center of pressure on the GTS model relative to that of the GCM geometry.

In the 7- by 10-Foot Wind Tunnel, the wind-averaged drag coefficients for the GTS and simplified-GCM geometries were 0.2770 and 0.3136, respectively. This difference can be attributed to the more complex tractor geometry, the gap in front of the belly box, and differing installation of the GCM configuration. The same simplified configuration in the 12-Foot Wind Tunnel yielded a wind-averaged drag of 0.3014, which differed from the 7- by 10-Foot result by just over the combined uncertainty of the two measurements. In addition to experimental uncertainty, installation differences were likely the cause of this discrepancy.

3.7 Data Set Discrepancies

Multiple Facilities. Although the GCM was tested at the same conditions in both the 7- by 10-Foot and 12-Foot Wind Tunnels, there was a significant difference between the wind-averaged drag for the extender baseline (config. 8). At Mach = 0.15 and Re = 1.1 million, the wind-averaged drag coefficients in the 7- by 10-Foot and 12-Foot Wind Tunnels were 0.4267 and 0.4313, respectively. These values differ by just less than observed repeatability of the 7- by 10-Foot data (±0.005), but two repeat runs in the 12-Foot fell outside of this range. Notable differences between the two installations are listed below:

1. Solid blockage. At zero yaw, the ratio of model projected area to wind tunnel cross section was 1.5% and 2.4% in the 12-Foot and 7- by 10-Foot Wind Tunnels, respectively. This will yield small differences in the streamlines around the model for the same configuration.

2. Static pressure reference. In both tunnels, the static pressure reference was chosen as a point on the test section wall. Due to the differences in test section geometry, the reference locations were not coincident (see Experimental Setup).

3. Model mounting post diameter and locations. Four posts were used to suspend the model in the test section in both wind tunnels. Due to the requirements of the 7- by 10-ft facility scale system and the 12-ft internal balance, the diameters and locations of the posts differed (see Experimental Setup).

4. Test-section boundary layer. A ground plane was installed in the 12-Foot Wind Tunnel to minimize the incident boundary layer and the model was mounted with the bottom of the wheels offset vertically by 3.8 mm. In the 7- by 10-Foot Wind Tunnel, no ground plane was installed and, to compensate for the measured displacement thickness of the boundary layer, the model was mounted 1.3 cm above the tunnel floor.

5. Inclination of the tractor. Because of the expected loads in the 7- by 10-Foot Wind Tunnel, more sensitive flexures were used to connect the tractor and trailer. As a result, the front wheels of the tractor were 6 mm lower than the rear wheels (i.e., the tractor had a nose-down inclination). The model was mounted nominally level in the 12-Foot Wind Tunnel.

6. Body-axis force and moment calculations. In the 12-Foot Wind Tunnel, the forces and moments were measured directly by an internal balance. In contrast, the same measurements in the 7- by 10-Foot Wind Tunnel were made by the facility scale system in the wind-axis coordinate system. This necessitated a coordinate-system transformation that, by definition, was sensitive to errors in yaw angle.

A comparison of the forces and moments for the best extender configuration (config. 8) in both facilities is presented in figure 57 for a Reynolds number of 1 million. The largest differences were seen within 5 deg of zero yaw for the normal force and pitching moment coefficients, likely due to the inclination of the tractor noted above. This may also explain the difference in the drag curves near zero yaw, while the observed asymmetry of the 7- by 10-ft results was likely a hysteresis effect. The yawing-moment coefficients compared favorably except at the higher angles where the effect of model blockage was most significant. Both the side-force and rolling-moment curves indicated a

small offset between facilities. As discussed above, numerical errors due to an offset in yaw angle may have affected the coordinate transformation of 7- by 10-ft data.

12-Ft Multiple Entries. In addition to the differing wind tunnels, two separate wind tunnel entries were conducted in the 12-Foot Wind Tunnel. The data for runs 200–250 were acquired over 3 months later than the first entry (up to run 59). Relative to the first entry, the wind-averaged drag coefficient from the second entry was over 0.01 higher for the baseline side and roof extender case (config. 8). This difference was approximately an order of magnitude higher than the expected uncertainty at the higher Reynolds numbers. Although the model was not completely removed from the test section, there were several differences between the model installations of the two entries. Possible contributions to the observed discrepancy are listed below in order of perceived importance:

1. Tractor re-installation. The last configuration of the first entry was a trailer-only case (i.e., the tractor had been removed). Therefore, it was possible that the tractor installation differed slightly between the two entries.

2. PIV mirrors. The second entry was mainly focused on particle image velocimetry measurements in the tractor-trailer gap and the trailer wake. During baseline repeat, a mirror was mounted on each of the tunnel walls. The mirrors extended vertically from the ground plane to the bottom of the side window and longitudinally from the rear of the model by approximately two trailer widths. Since the mirrors were nominally flush with the circular tunnel wall, their effect was likely minimal.

3. Model height. The height of the model above the ground plane differed by less than 0.5 mm from that of the first entry, so this is not a likely source of the discrepancy.

A comparison of the drag coefficients for the two entries (fig. 58(a)) showed a relatively constant drag increase at all yaw angles for the second entry relative to the first. The magnitude of the yawing moment, in contrast, was slightly reduced at the higher yaw angles (fig. 58(b)). The change in component drag and yawing-moment coefficients between the two entries (fig. 59) helped to identify the source of observed differences. Although both tractor and trailer contributed to the discrepancy, the trailer differences appeared to dominate. To compare with the drag measured by the internal balance, a drag coefficient was calculated using the average trailer base pressures. Although there were limited pressure taps clustered near the edge on only one side of the trailer base, an average of the trailer base pressures should provide an approximation of the trailer drag. Relative to the first entry, the resulting comparison (fig. 60) indicated that the drag coefficients from the base pressures were of the same magnitude as those of the internal balance. This correlation ruled out possible internal balance problems and confirmed that the measured discrepancy was likely due to installation differences between the two entries. To account for this discrepancy in appendix B, the tabulated differences in wind-averaged drag for 2nd-entry configurations were computed relative to the 2nd-entry baseline (run 242).

4.0 SUMMARY

The Generic Conventional Model was studied experimentally in the 7- by 10-Foot and 12-Foot Wind Tunnels at Ames Research Center. This 1:8-scale model included a tractor-trailer gap and a simplified conventional tractor geometry to facilitate computational modeling. Measurements were conducted at a Reynolds number of 1.1 million in the 7- by 10-Foot Wind Tunnel and up to 6.2 million (equivalent to full-scale Reynolds numbers at highway speeds) in the 12-Foot Pressure Wind Tunnel. The measurements included overall and component forces and moments, static and dynamic surface pressures, and three-component velocity data using particle image velocimetry. This summary report presents details of the model installation in both tunnels, an overview of the extensive database, and an analysis of the observed discrepancies between experiments. Numerous drag-reduction devices were studied on both the tractor and trailer bases as well as on the trailer underbody. The most promising and practical devices include the tractor side and roof extenders, the trailer side skirts, and the trailer base flaps. Using the standard algorithm to account for crosswind, a wind-averaged drag coefficient was computed for all configurations tested and tabulated in an appendix for ease of comparison. This database is publicly available for further analysis.

5.0 REFERENCES

1. McCallen, R.; Flowers, D.; Dunn, T.; Owens, J.; Leonard, A.; Brady, M.; Brownad, F.; Hammache, M.; Salari, K.; Rutledge, W.; Ross, J.; Storms, B.; Heineck, J. T.; Driver, D.; Bell, J.; Zilliac, G.; and Walker, S.: Aerodynamic Drag of Heavy Vehicles (Class 7–8): Simulation and Benchmarking. 2000-01-2209, SAE Gov/Industry Meeting, Washington, D.C., June 19–21, 2000.
2. Cooper, K. R.: Truck Aerodynamics Reborn – Lessons from the Past. SAE Paper 2003-01-3376, November, 2003.
3. Cooper, K.: The Wind Tunnel Testing of Heavy Trucks to Reduce Fuel Consumption. SAE Paper 821285, November, 1982.
4. Croll, R. H.; Gutierrez, W. T.; Hassan, B.; Suazo, J. E.; and Riggins, A. J.: Experimental Investigation of the Ground Transportation Systems (GTS) Project for Heavy Vehicle Drag Reduction. SAE Paper 960907, February, 1996.
5. Storms, B. L.; Ross, J. C.; Heineck, J. T.; Walker, S. M.; Driver, D. M.; and Zilliac, G. G.: An Experimental Study of the Ground Transportation System (GTS) Model in the NASA Ames 7- by 10-Foot Wind Tunnel. NASA/TM-2001-209621, February, 2001.
6. Hammache, M.; Michaelian, M.; and Browand, F.: Aerodynamic Forces on Truck Models, Including Two Trucks in Tandem. SAE Paper 2002-01-0530, March, 2002.
7. Heineck, J. T.; Walker, S. M.; and Satran, D.: The Measurement of Wake and Gap Flows of the Generic Conventional Truck Model (GCM) using Three-Component PIV. The Aerodynamics of Heavy Vehicles: Trucks, Buses and Trains, Monterey-Pacific Grove, CA, Dec., 2002.

8. Heineck, J. T.; Walker, S. M.; and Yaste, D. M.: The Development of a 3C-PIV System for the 12-Foot Pressure Tunnel at NASA Ames Research Center. International Congress on Instrumentation of Aerospace Simulation Facilities, Goettingen, Germany, August, 2003.

9. Storms, B. L.; Satran, D. R.; Heineck, J. T.; and Walker, S. M.: A Study of Reynolds Number Effects and Drag-Reduction Concepts on a Generic Tractor-Trailer. AIAA Paper 2004-2251, June, 2004.

10. Cooper, K. R; and Leuschen, J.: Model and Full-Scale Wind Tunnel Tests of Second-Generation Aerodynamic Fuel Saving Devices for Tractor-Trailers. SAE Paper 2005-01-3512, November, 2005.

11. SAE Wind Tunnel Test Procedure for Trucks and Buses. SAE J1252 JUL81, SAE Recommended Practice, July, 1981.

12. Storms, B. L.; Satran, D. R.; Heineck, J. T.; and Walker, S. M.: Detailed Experimental Results of Drag-Reduction Concepts on a Generic Tractor-Trailer. SAE Paper 2005-01-3525, November, 2005.

13. Simiu, E.; and Scanlan, R.: Wind Effects on Structures. Third Edition, John Wiley & Sons, Inc., New York, N. Y., 1996, pg. 152.

14. Browand, F.; and Radovich, C.: Fuel Savings by Means of Flaps Attached to the Base of a Trailer: Field Test Results. USC Research Report, May, 2004.

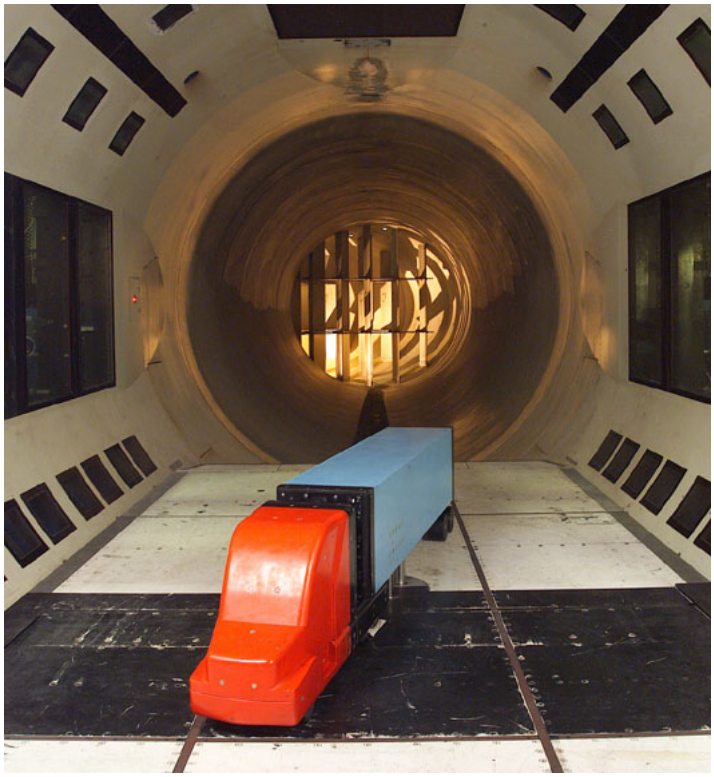

Figure 1. The Generic Conventional Model installed in the 12-Foot Pressure Wind Tunnel.

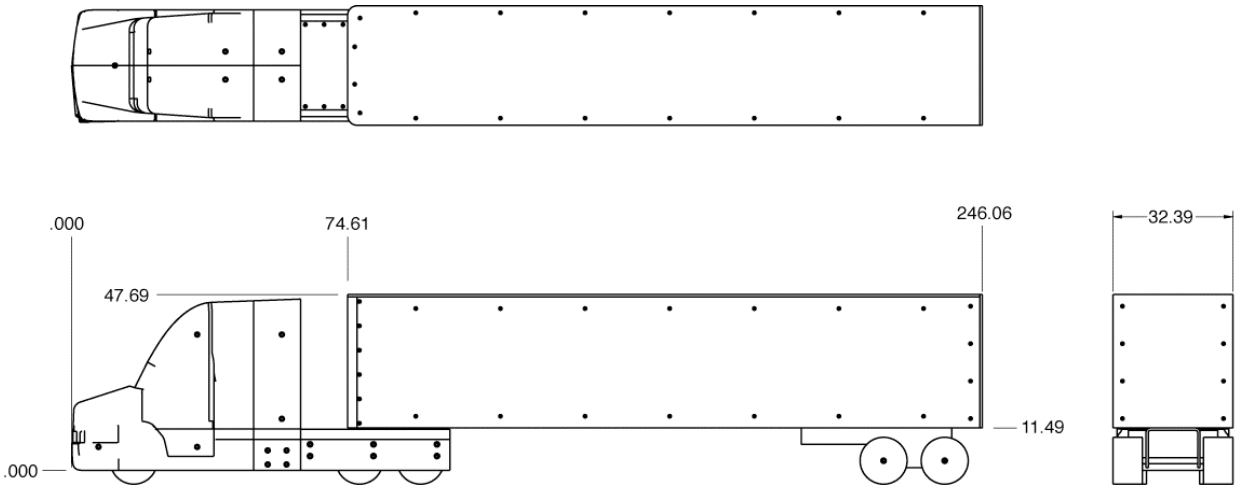

Figure 2. Three-view drawing of Generic Conventional Model (measurements in cm).

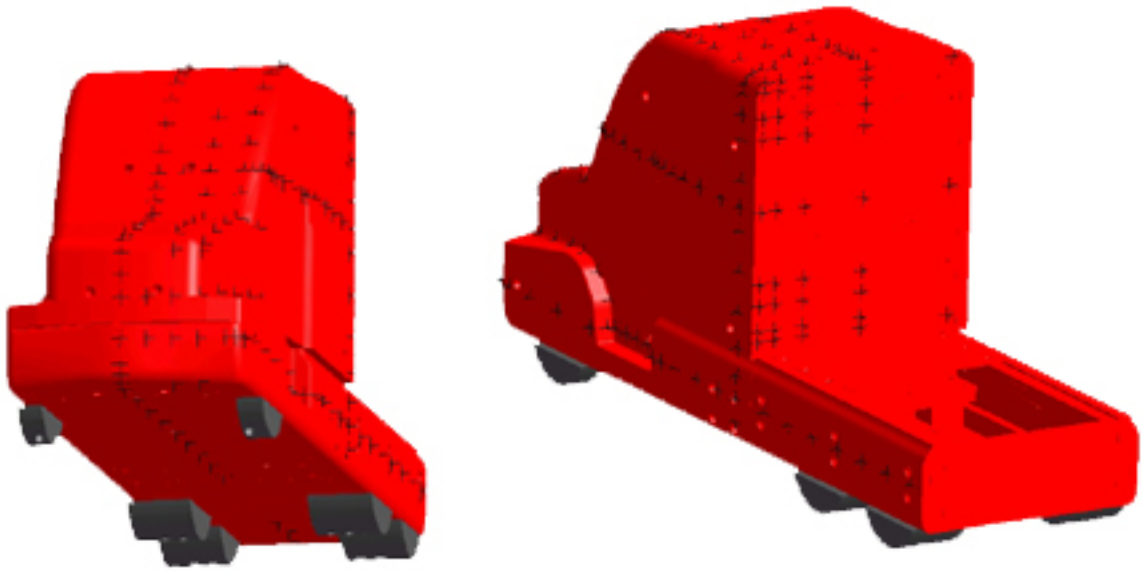

Figure 3. Relative pressure-tap locations on GCM tractor.

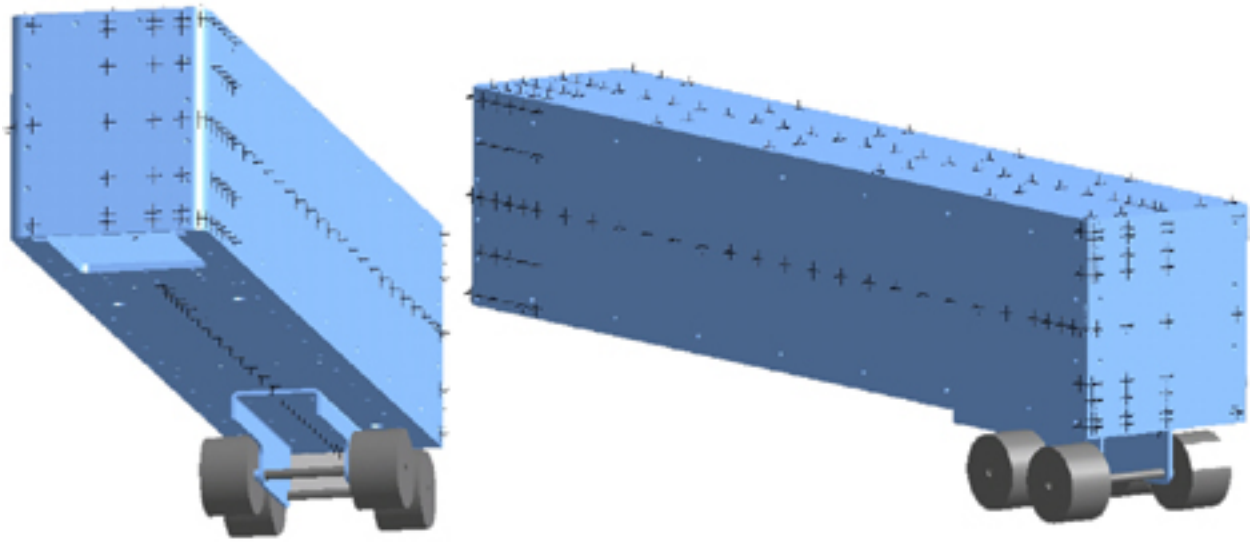

Figure 4. Relative pressure-tap locations on GCM trailer.

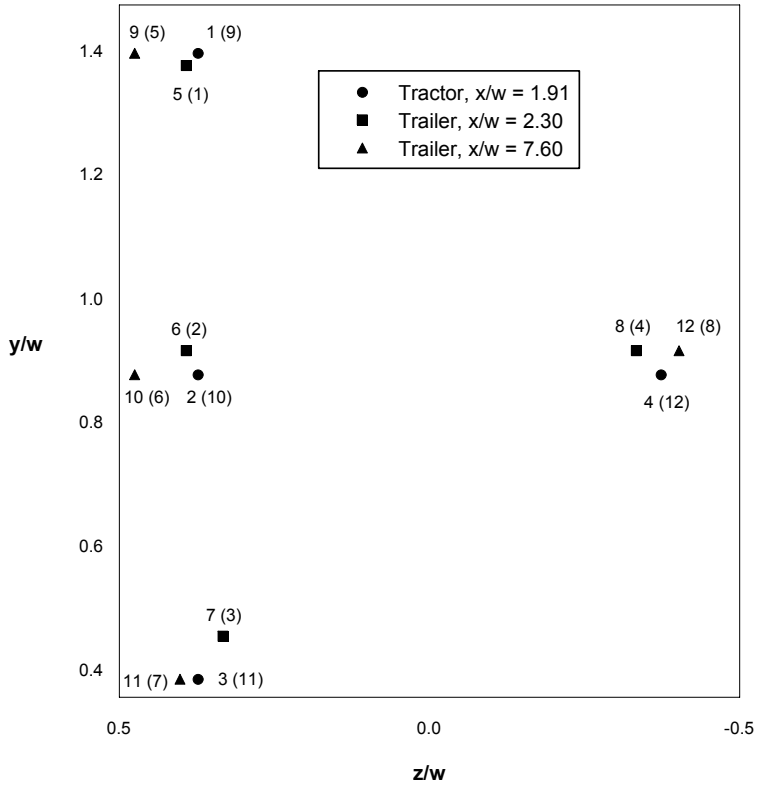

Figure 5. Dynamic sensor locations on back of tractor and front/back of trailer. Sensor numbering refers to 12-Foot and 7- by 10-Foot Wind Tunnels with the latter in parentheses.

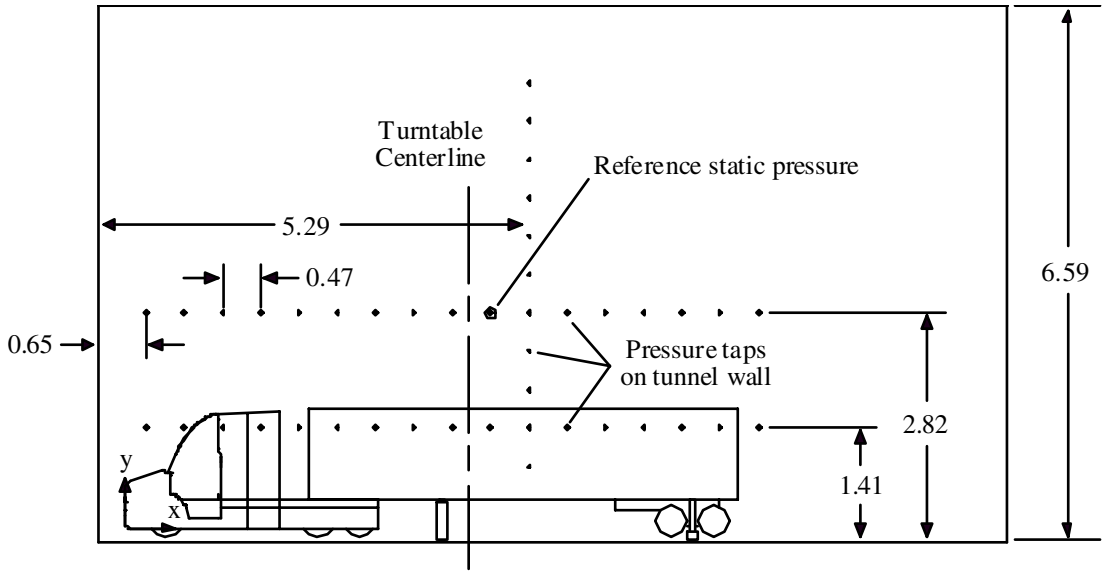

Figure 6. Relative locations of pressure taps on test section wall of the 7- by 10-Foot Wind Tunnel. All measurements are normalized by the trailer width.

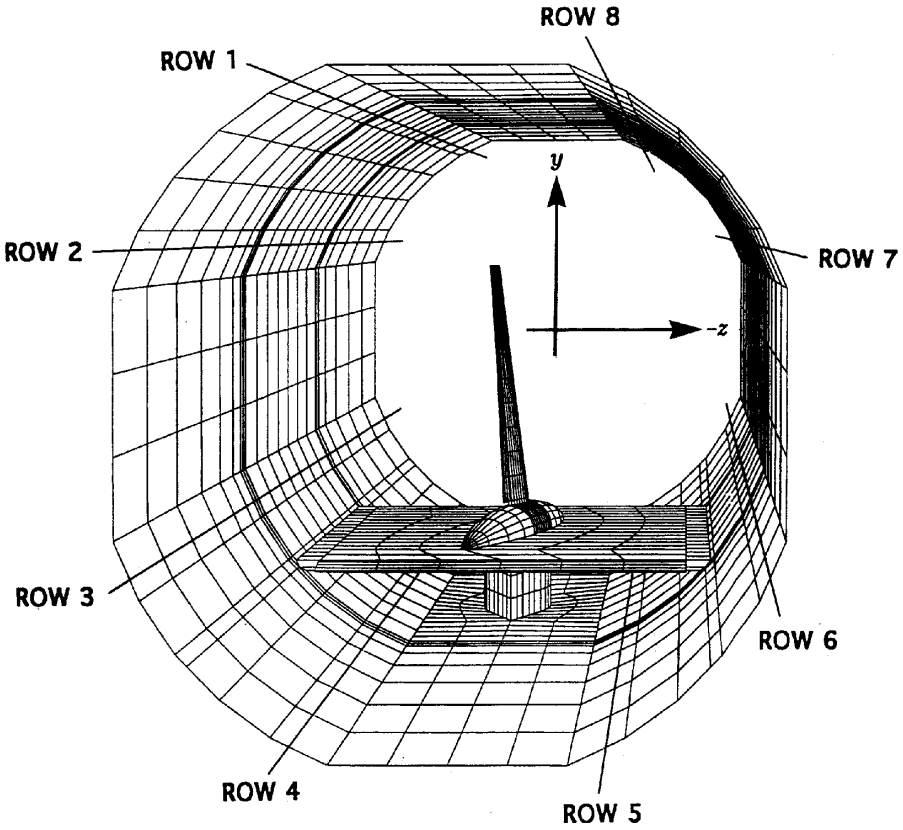

Figure 7. Typical image-plane installation in 12-Foot Pressure Wind Tunnel. Relative locations of wall pressure-tap rows are also indicated.

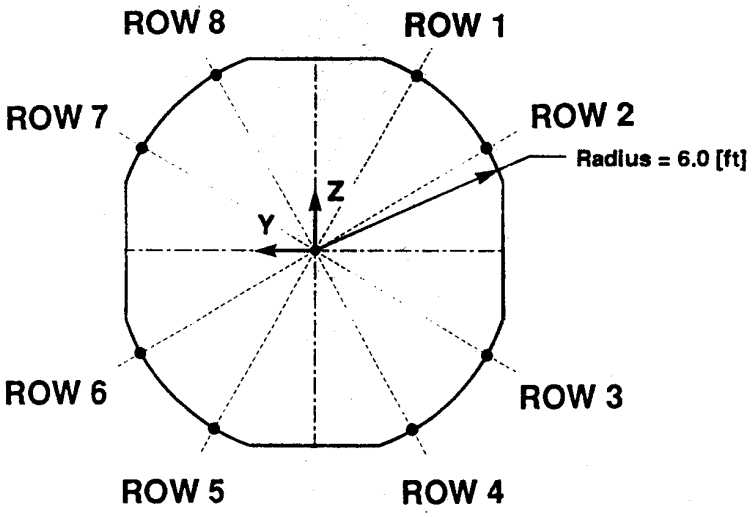

Figure 8. Pressure-tap row locations in 12-Foot Pressure Wind Tunnel. Note that y- and z-axes are swapped (i.e., y-axis vertical) for the GCM installation.

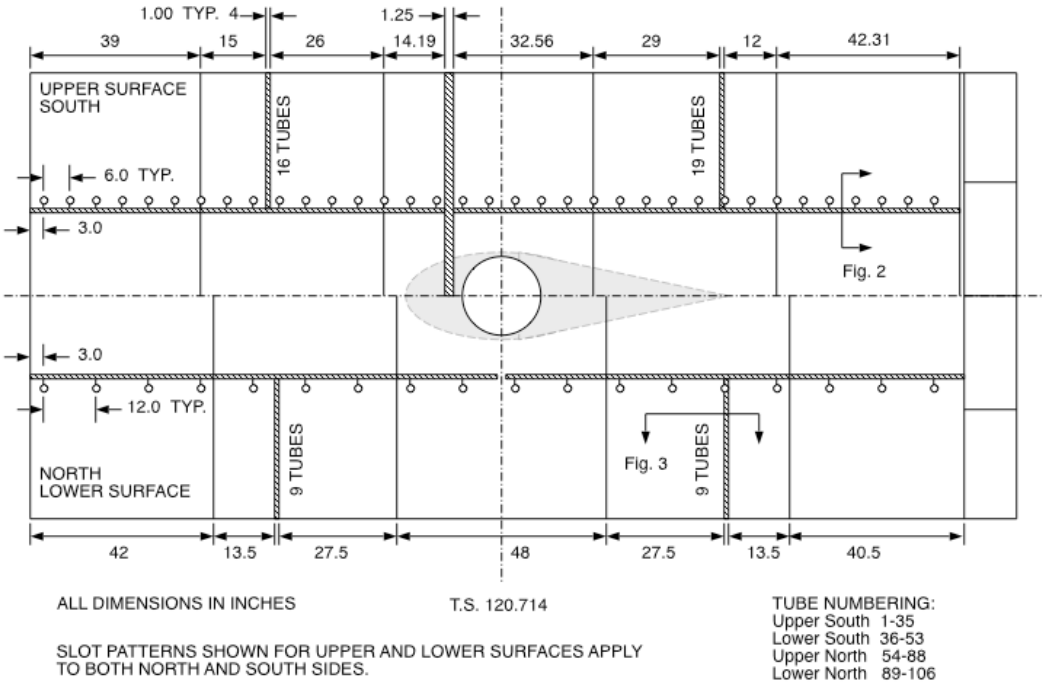

Figure 9. Pressure-tap locations on the image plane in the 12-Foot Pressure Wind Tunnel.

Figure 10. Tractor-trailer geometry tested by National Research Council of Canada (ref. 10). Standard aero package and side extenders are blue and red, respectively.

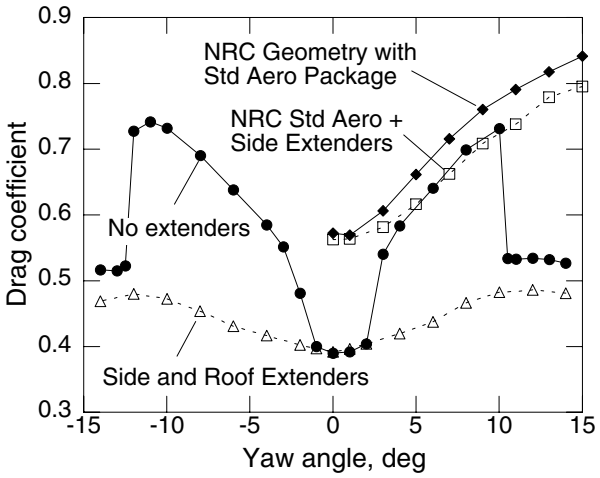

Figure 11. Comparison between GCM (12-ft, Re = 1 million) and more realistic NRC geometry (ref. 10) with and without tractor side extenders.

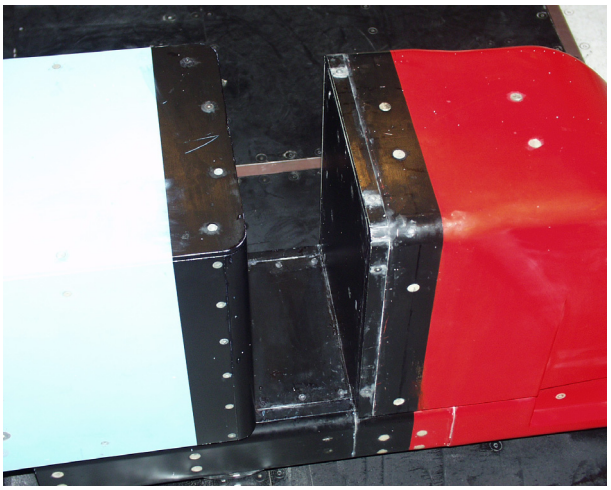

a) No extenders ($\Delta \bar{C}_D = +0.0600$)

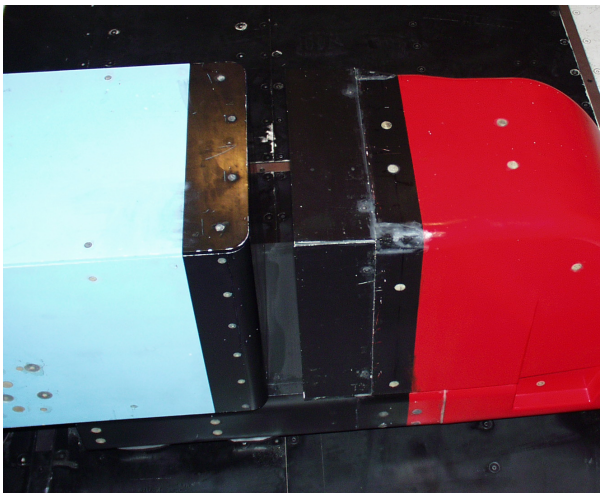

b) Side & roof extenders (60% gap)

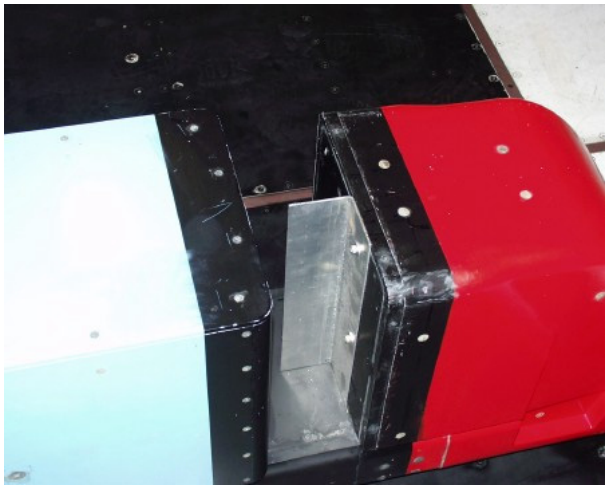

c) Cab splitter ($\Delta \bar{C}_D = +0.0501$)

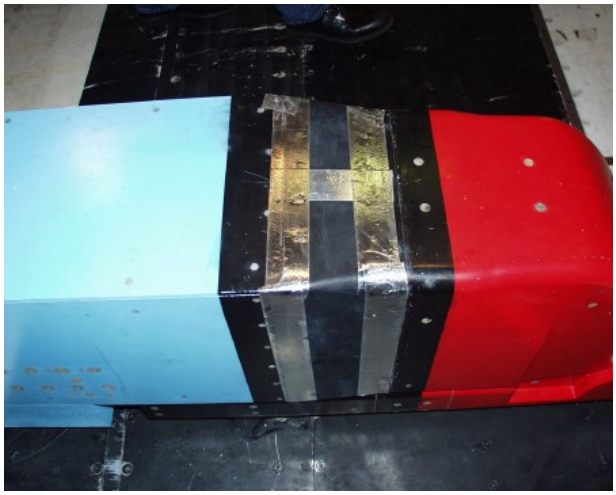

d) Gap filler ($\Delta \bar{C}_D = +0.0005$)

Figure 12. Close-up of tractor-trailer gap with and without add-ons. Change in wind-averaged drag relative to 60%-gap side and roof extenders (config. 8).

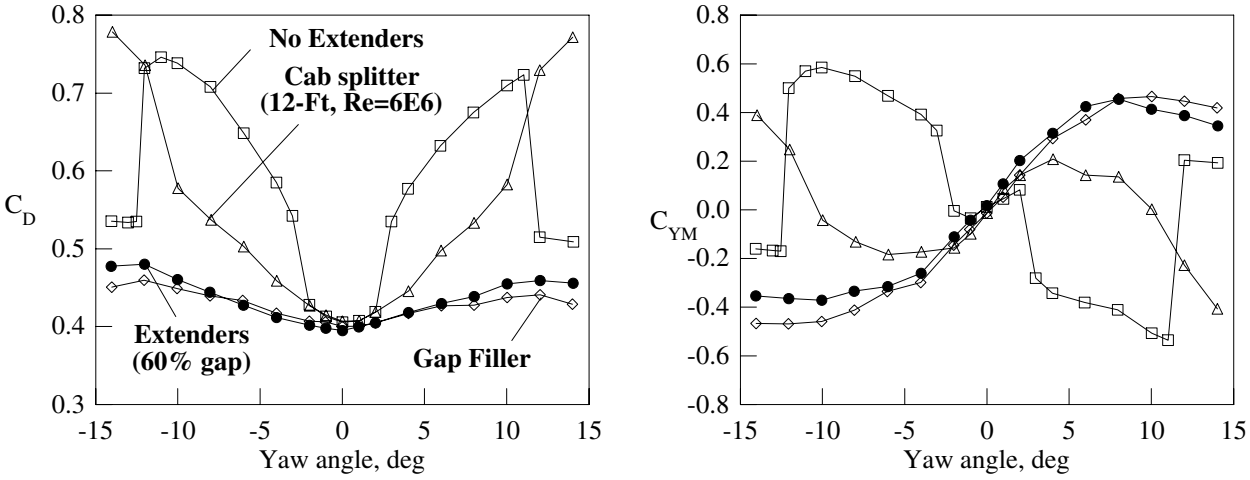

a) Drag coefficient

b) Yawing-moment coefficient

Figure 13. Effect of tractor add-ons on body-axis drag and yawing moment coefficients. Unless specified, data are from 7- by 10-Foot Wind Tunnel at Re = 1 million.

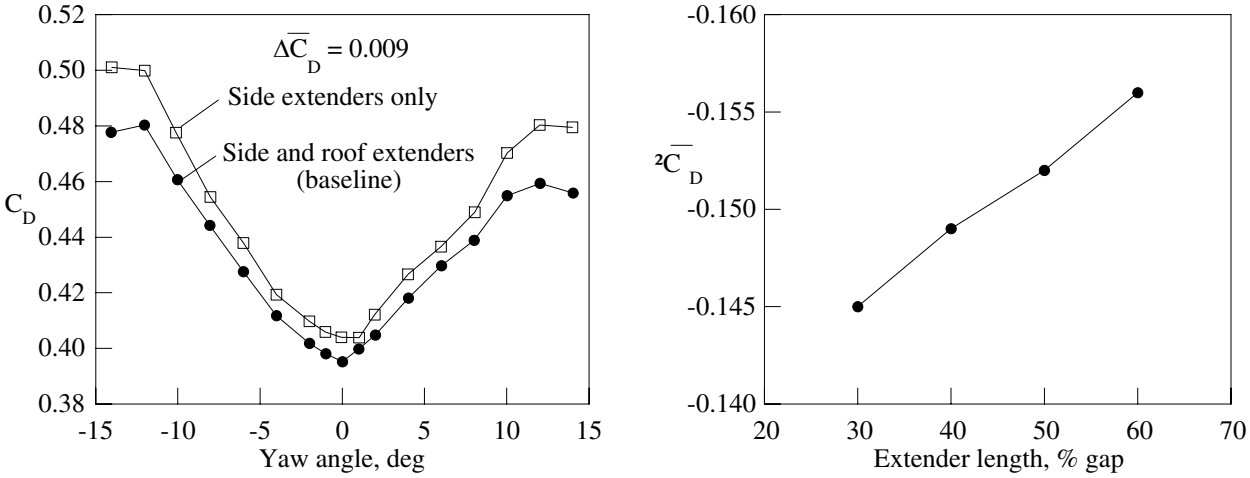

Figure 14. Effect of roof extender on drag coefficient (60%-gap extenders, Re = 1.1E6, 7x10-Foot Wind Tunnel).

Figure 15. Wind-averaged drag reduction due to side and roof extenders at Re = 6E6 (relative to no-extender configuration).

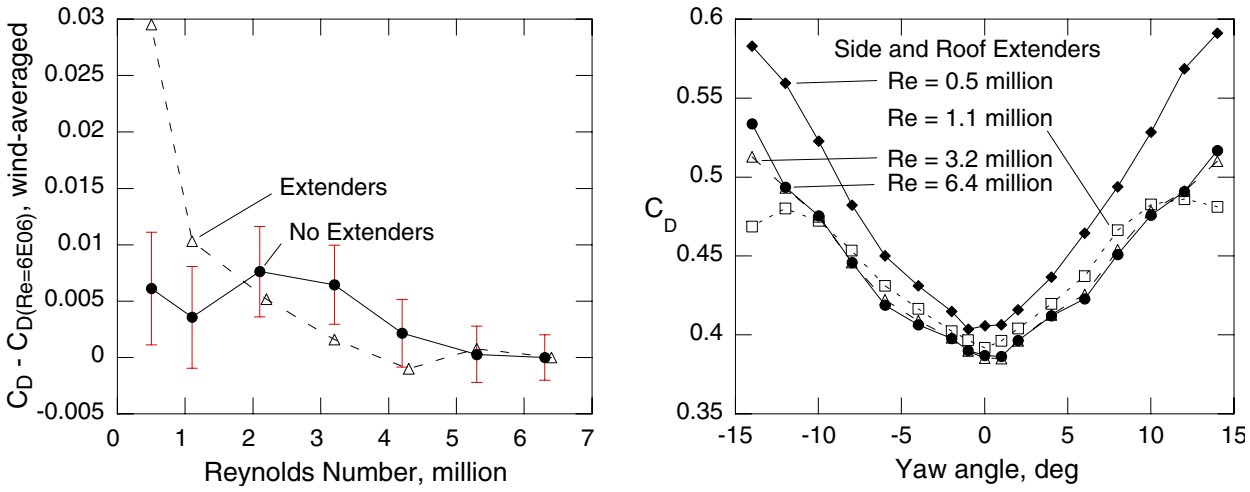

a) Difference in wind-averaged drag

b) Drag curves with extenders

Figure 16. Reynolds number sensitivity of GCM with and without 60%-gap side and roof extenders (12-Foot Wind Tunnel).

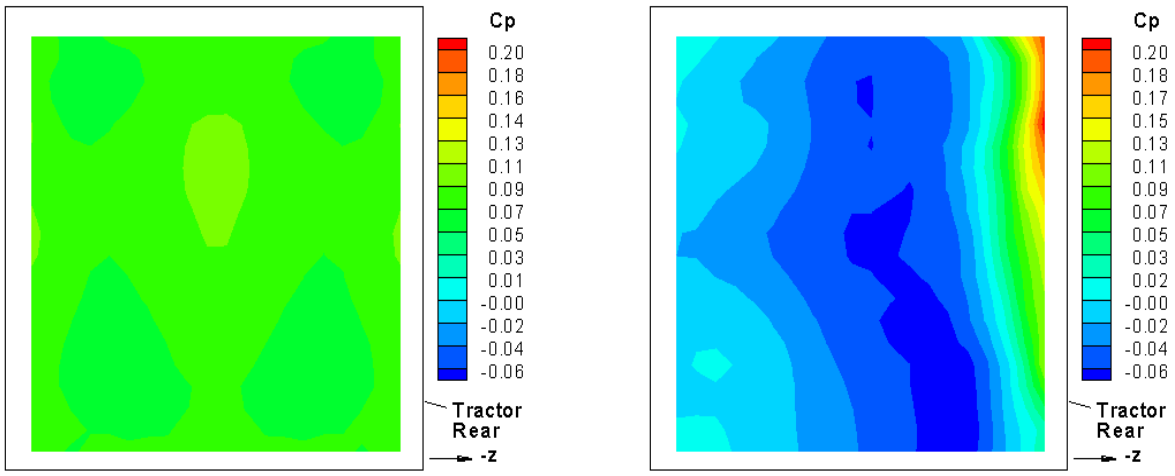

a) Ψ = 0 deg

b) Ψ = 10 deg

Figure 17. Pressure coefficient contours on the back of the tractor with 0.6g side and roof extenders, Re = 6 million. Symmetry assumed for zero yaw. For Ψ = 10°, right half of image represents data at Ψ = –10°.

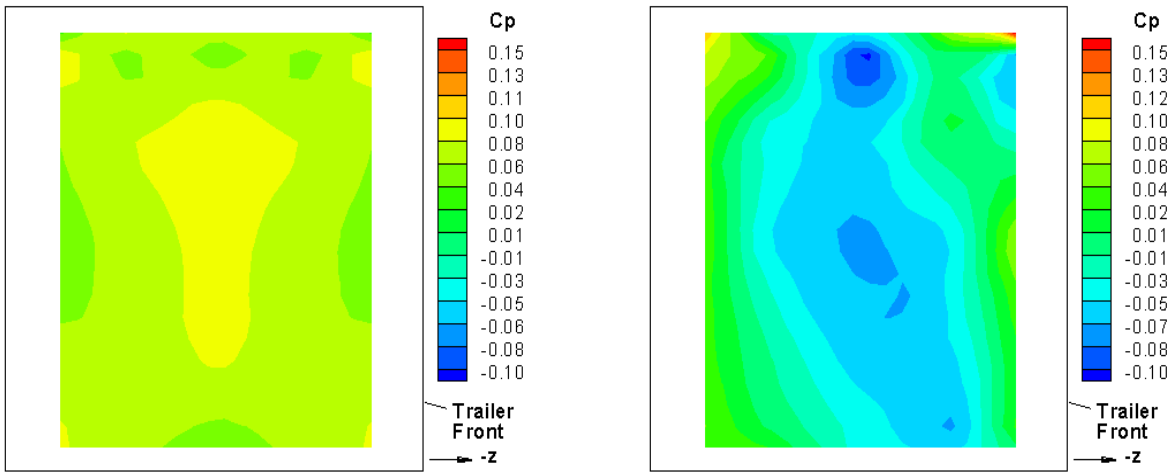

a) Ψ = 0 deg b) Ψ = 10 deg

Figure 18. Pressure coefficient contours on the front of the trailer with 0.6g side and roof extenders, Re = 6 million.

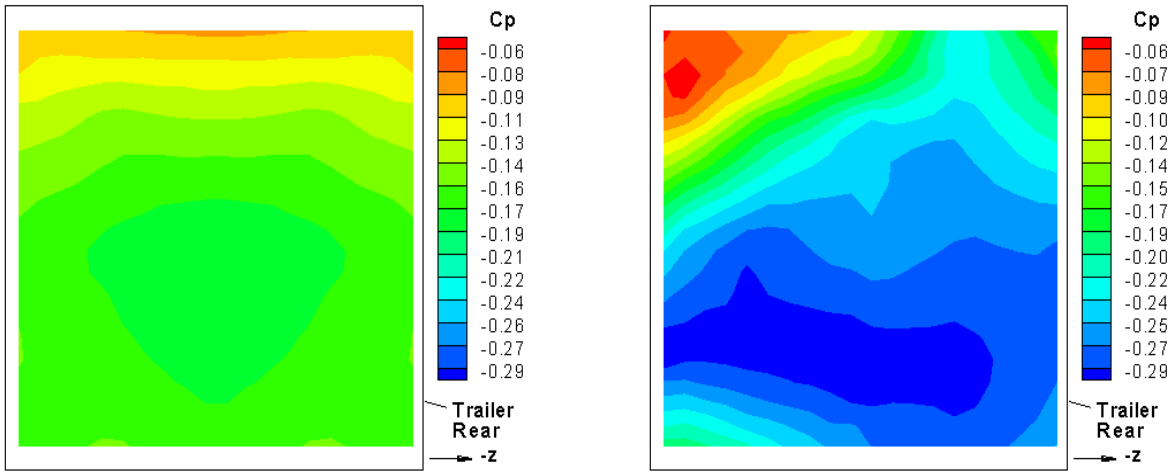

a) Ψ = 0 deg b) Ψ = 10 deg

Figure 19. Pressure coefficient contours on the back of trailer with 0.6g side and roof extenders, Re = 6 million.

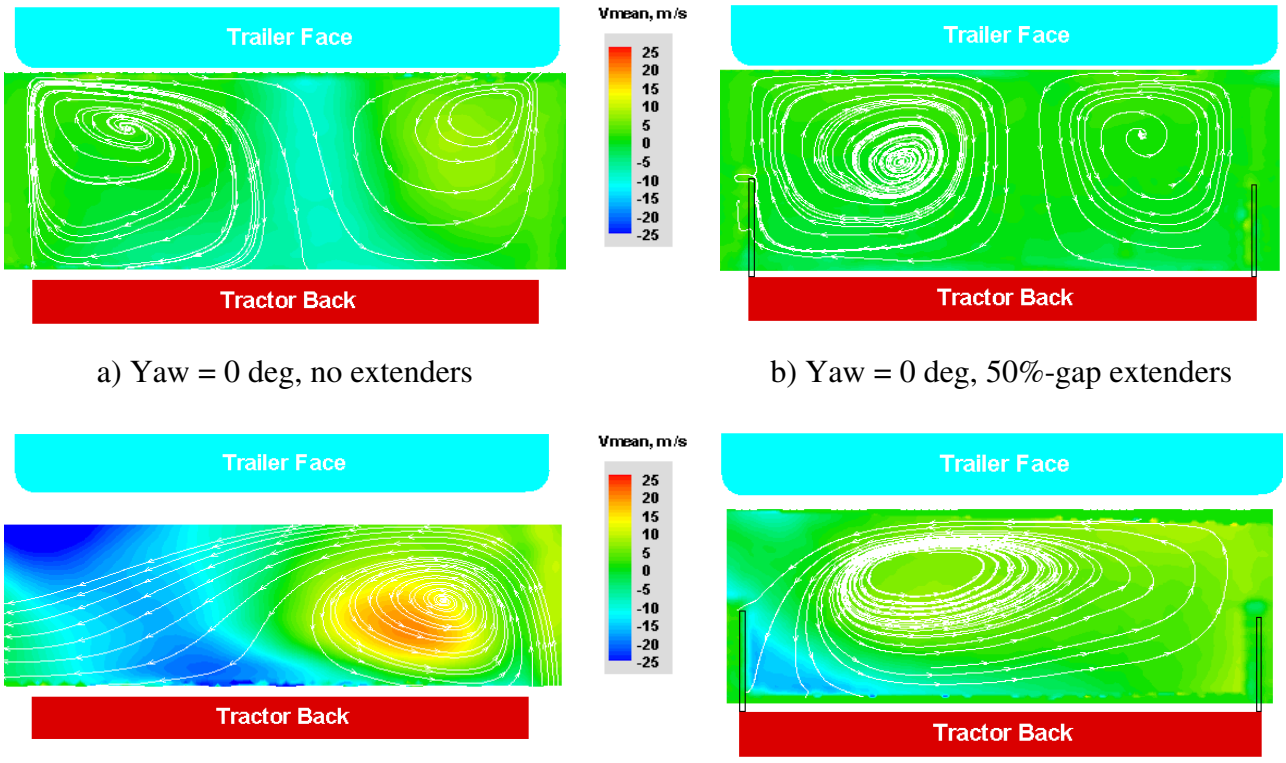

a) Yaw = 0 deg, no extenders

b) Yaw = 0 deg, 50%-gap extenders

c) Yaw = 10 deg, no extenders

d) Yaw = 10 deg, 50%-gap extenders

Figure 20. Particle image velocimetry data in the tractor-trailer gap with and without 50%-gap side extenders. Images are shaded by out-of-plane velocity (positive vertically up) and freestream flow is from bottom to top of the page (7x10-Foot Wind Tunnel, Re = 1 million).

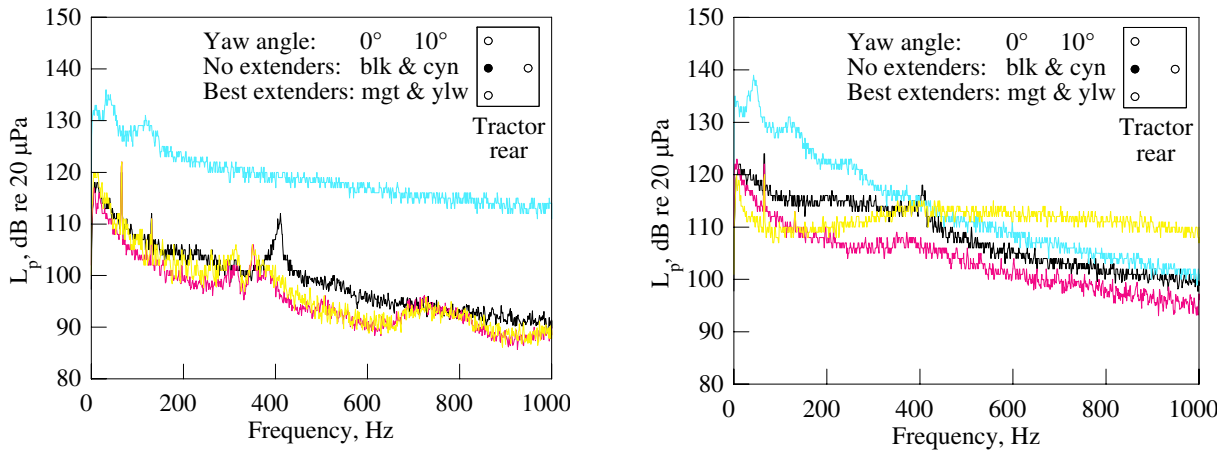

a) Tractor rear

b) Trailer front

Figure 21. Effect of tractor side and roof extenders on dynamic pressure spectra for mid-height, left-side sensor only (12-Foot Wind Tunnel, Re = 6 million).

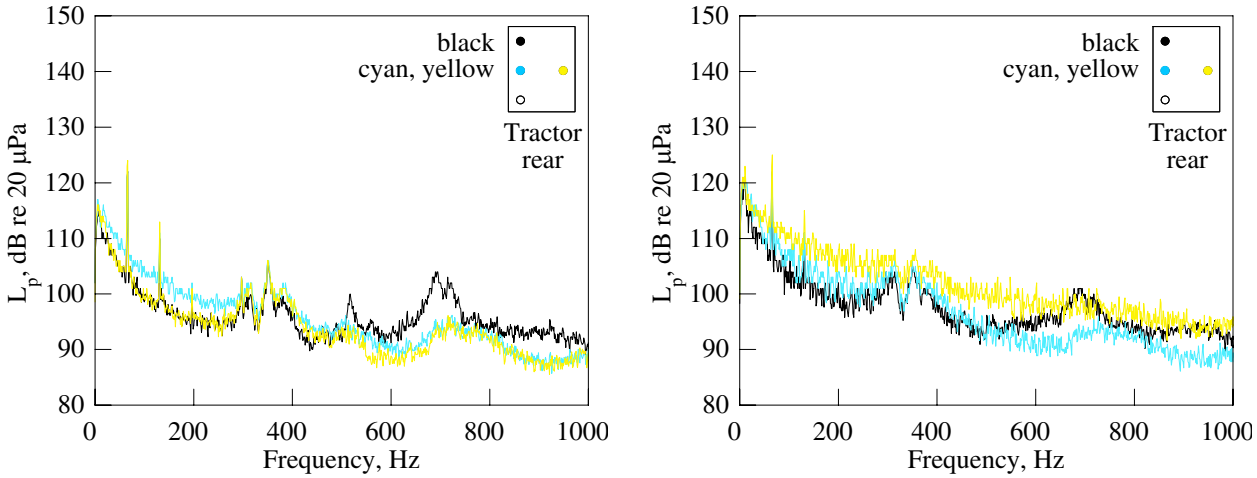

a) 0 deg b) 10 deg

Figure 22. Effect of yaw angle and sensor position on dynamic pressure spectra with 60%-gap side and roof extenders, tractor rear, Re = 6 million (bottom sensor was inoperable).

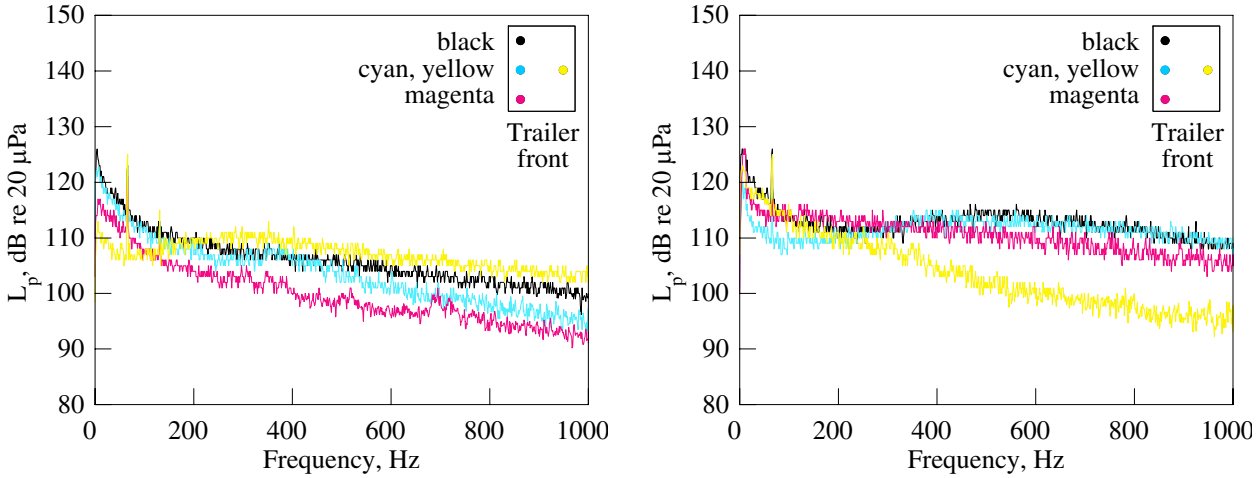

a) 0 deg b) 10 deg

Figure 23. Effect of yaw angle and sensor position on dynamic pressure spectra with 60%-gap side and roof extenders, trailer front, Re = 6 million.

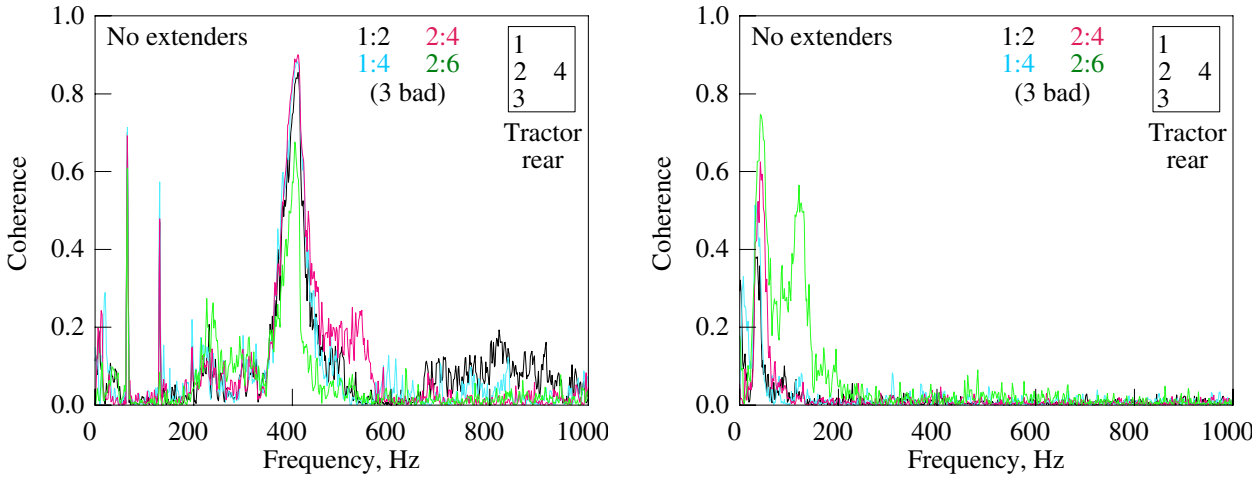

a) 0 deg b) 10 deg

Figure 24. Dynamic-pressure signal coherence between neighboring sensors on the rear of the tractor without side and roof extenders, Re = 6 million.

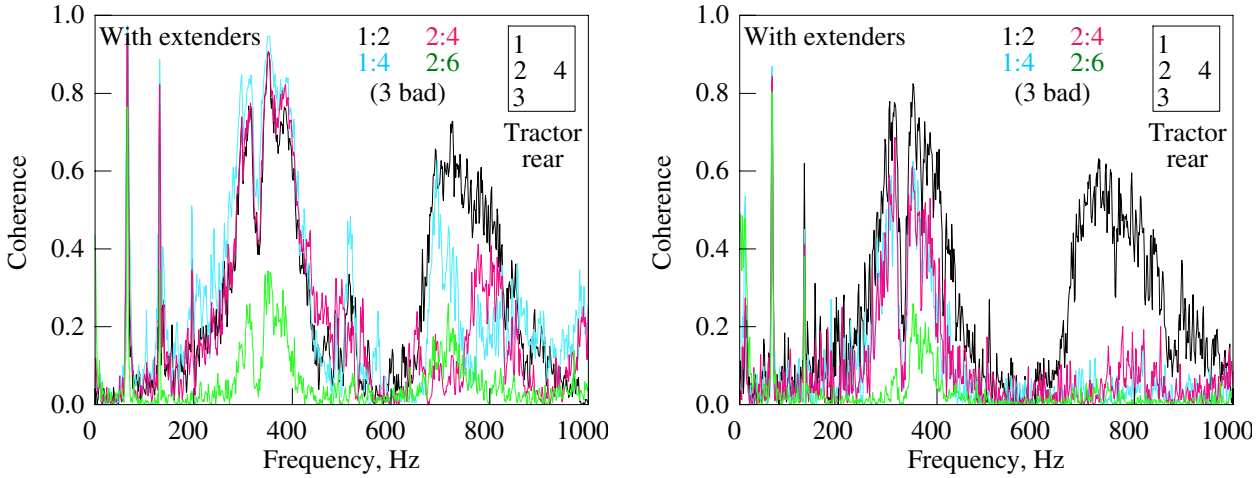

a) 0 deg b) 10 deg

Figure 25. Dynamic-pressure signal coherence between neighboring sensors on the rear of the tractor with 60%-gap side and roof extenders, Re = 6 million.

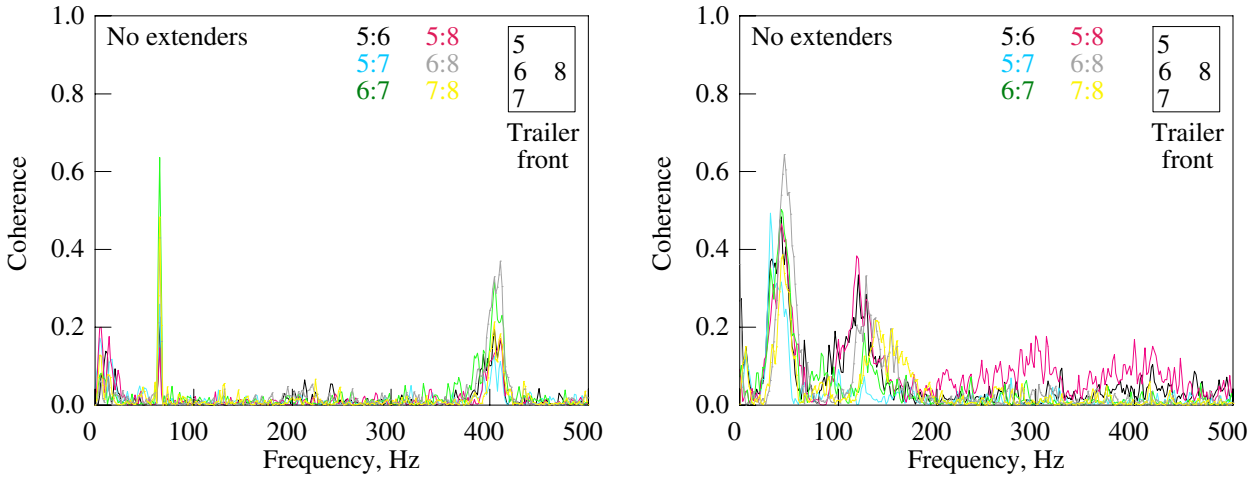

a) 0 deg b) 10 deg

Figure 26. Dynamic-pressure signal coherence between neighboring sensors on the front of the trailer without side and roof extenders, Re = 6 million.

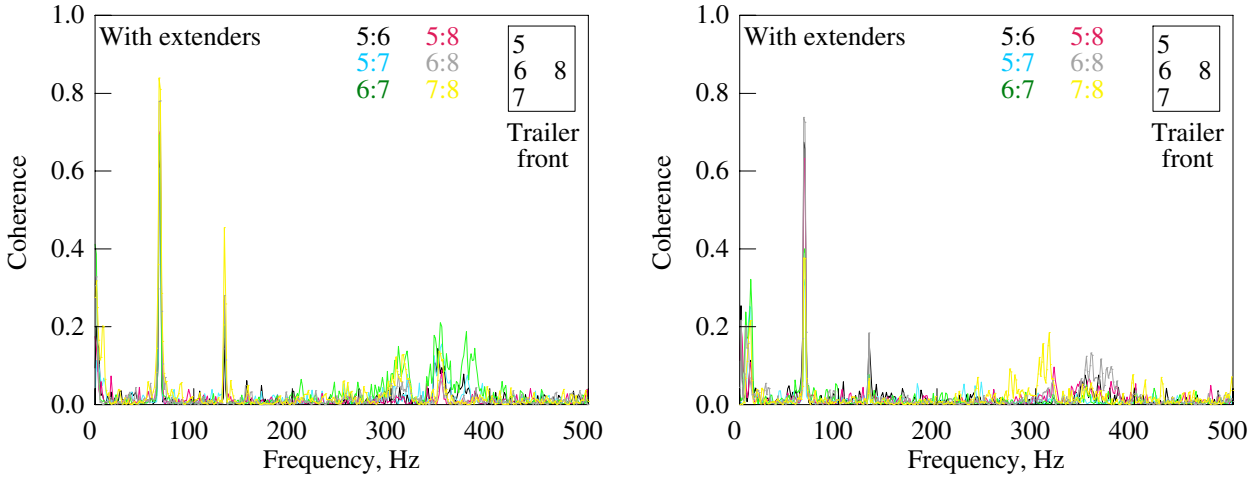

a) 0 deg b) 10 deg

Figure 27. Dynamic-pressure signal coherence between neighboring sensors on the front of the trailer with 60%-gap side and roof extenders, Re = 6 million.

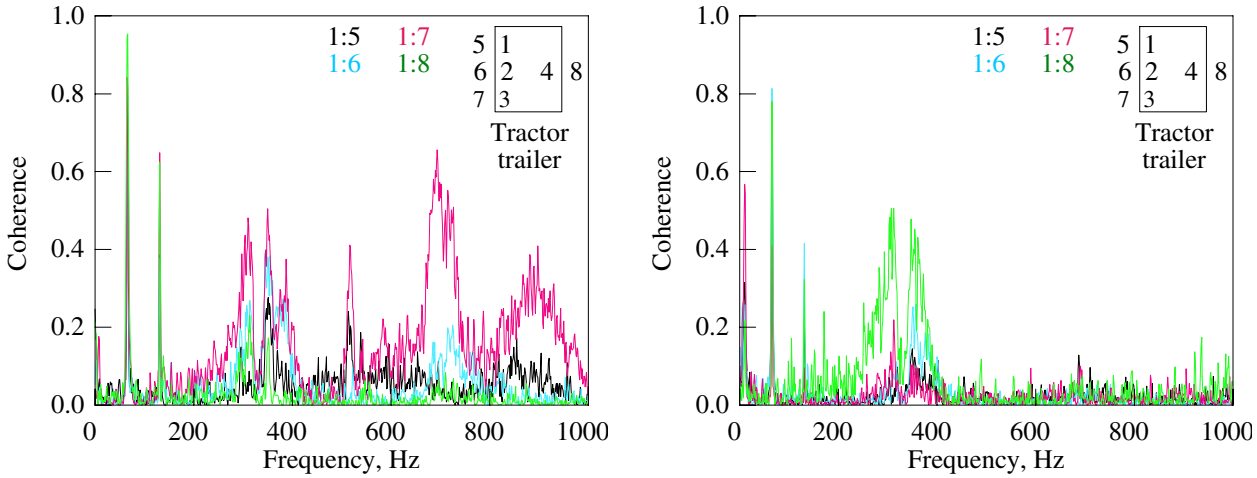

a) 0 deg b) 10 deg

Figure 28. Dynamic-pressure signal coherence between tractor sensor #1 and trailer sensors in the gap region with 60%-gap side and roof extenders, Re = 6 million.

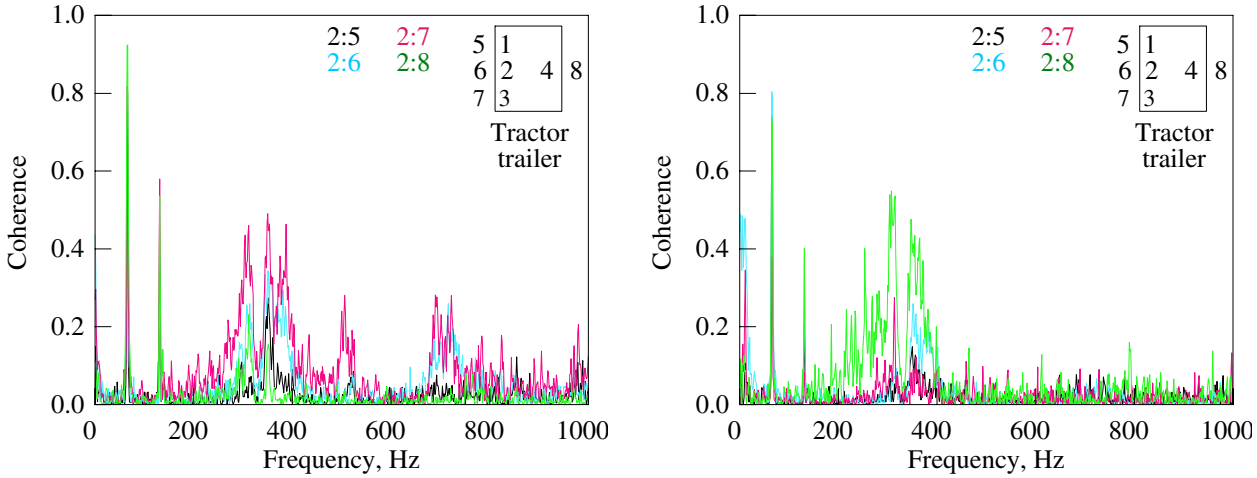

a) 0 deg b) 10 deg

Figure 29. Dynamic-pressure signal coherence between tractor sensor #2 and trailer sensors in the gap region with 60%-gap side and roof extenders, Re = 6 million.

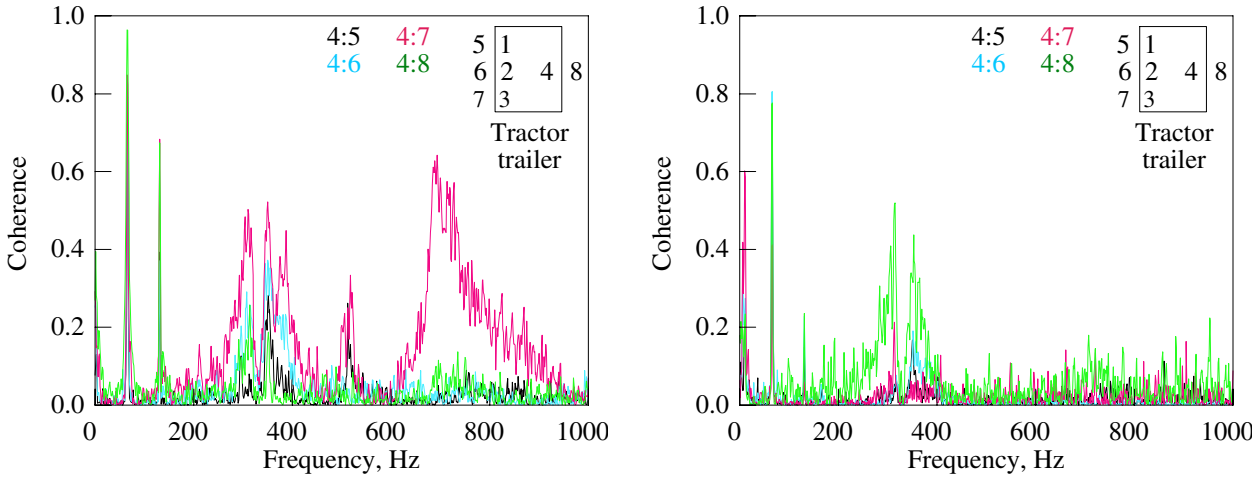

a) 0 deg

b) 10 deg

Figure 30. Dynamic-pressure signal coherence between tractor sensor #4 and trailer sensors in the gap region with 60%-gap side and roof extenders, Re = 6 million.

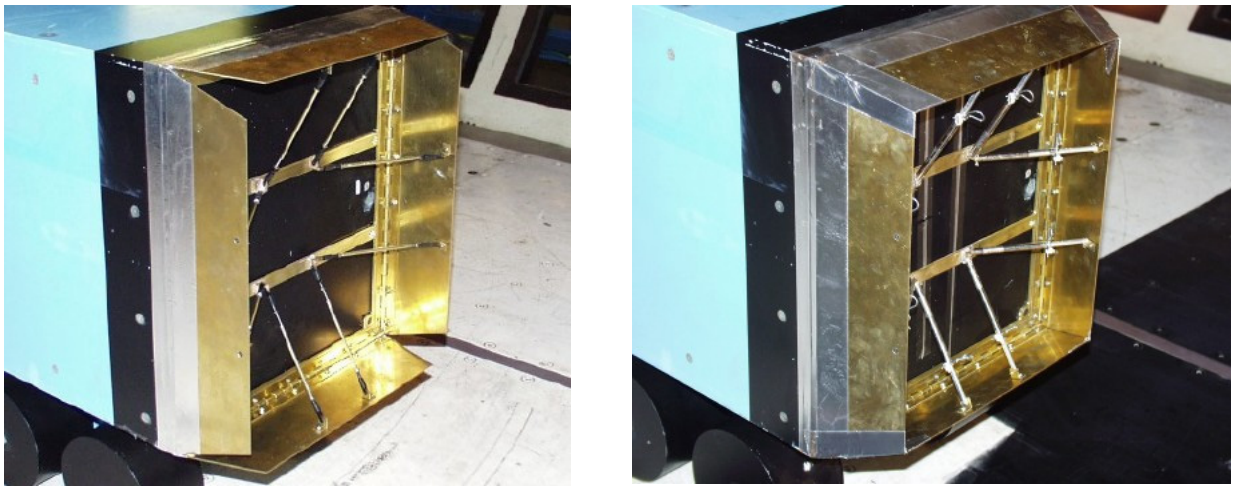

a) 8-deg flaps ($\Delta \bar{C}_D = -0.0400$)

b) 20-deg flaps ($\Delta \bar{C}_D = -0.0855$)

Figure 31. Base flaps installed on trailer base. Change in wind-averaged drag relative to 60%-gap side and roof extenders (config. 8).

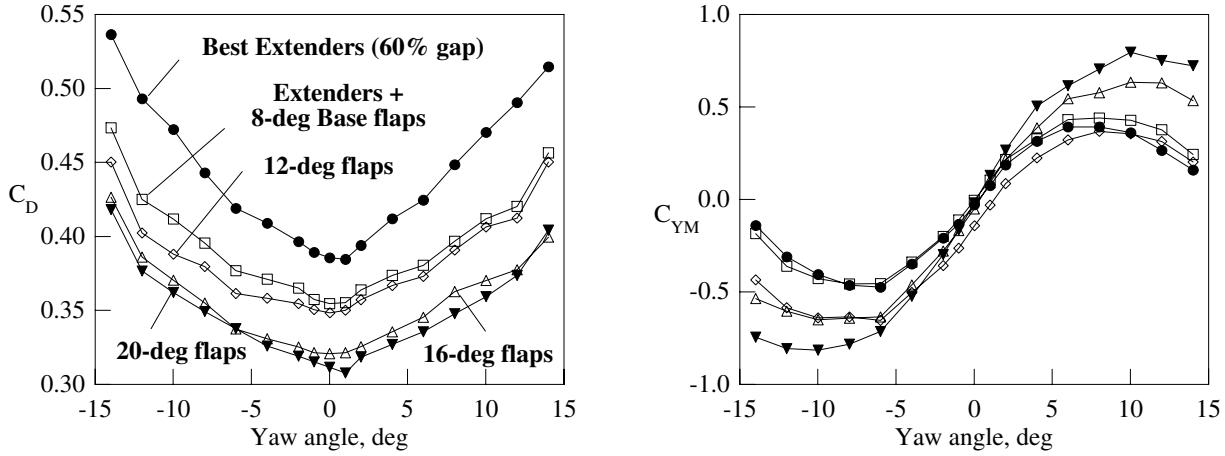

a) Drag coefficient b) Yawing-moment coefficient

Figure 32. Effect of trailer base flaps on body-axis drag and yawing moment coefficients. Unless otherwise specified, data are from 12-Foot Wind Tunnel at Re = 6 million.

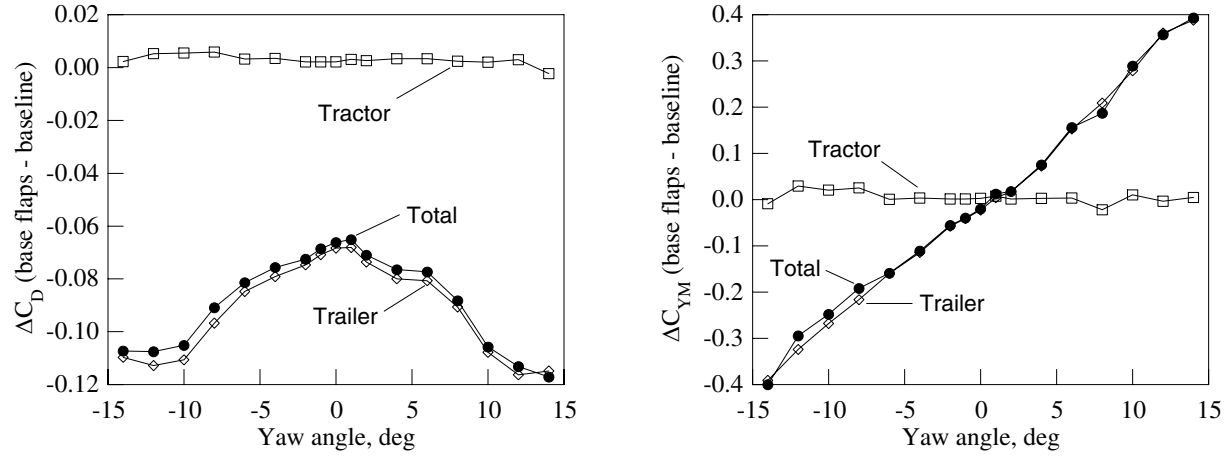

Figure 33. Effect of 16-deg base flaps on component drag and yawing-moment (Re = 6E06).

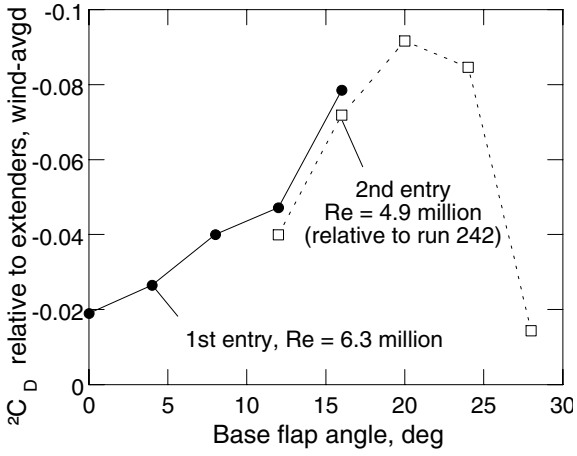

Figure 34. Effect of base-flap angle on wind-averaged drag reduction.

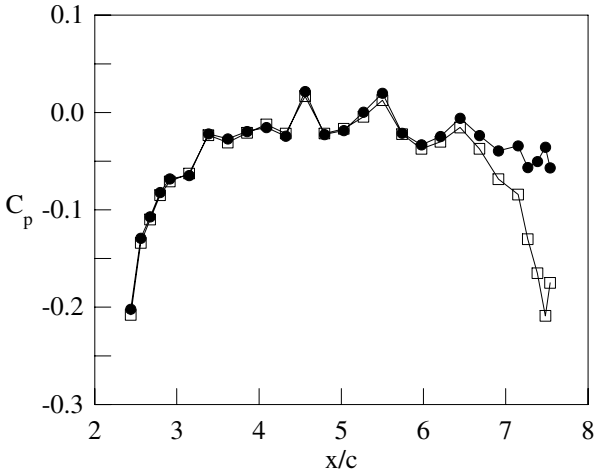

a) Ψ = 0°

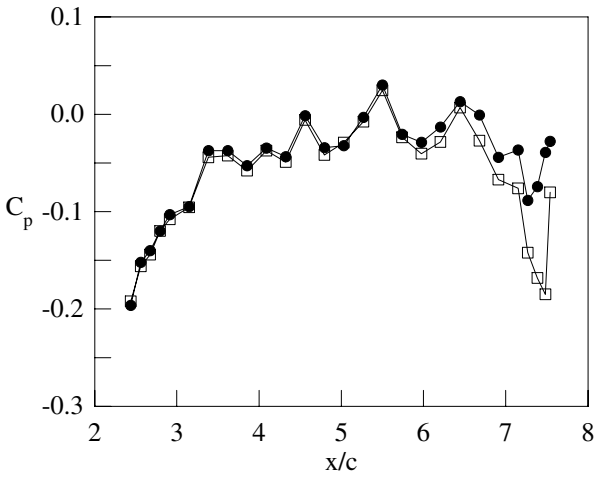

b) Ψ = 10°

Figure 35. Effect of 16-deg base flaps on trailer top centerline pressure coefficients, z/w = 0.0 (solid: baseline, open: base flaps, Re = 6 million).

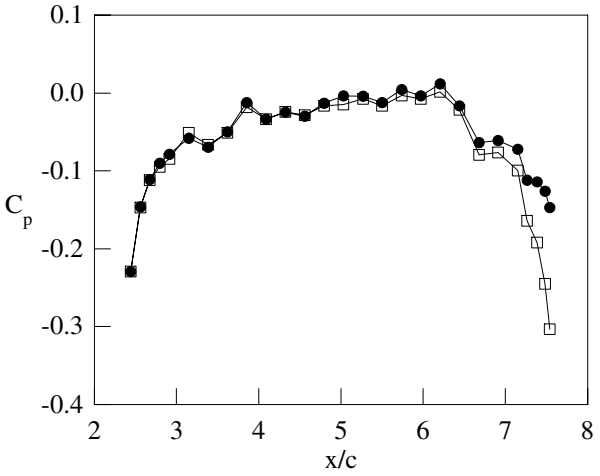

a) Ψ = 0°

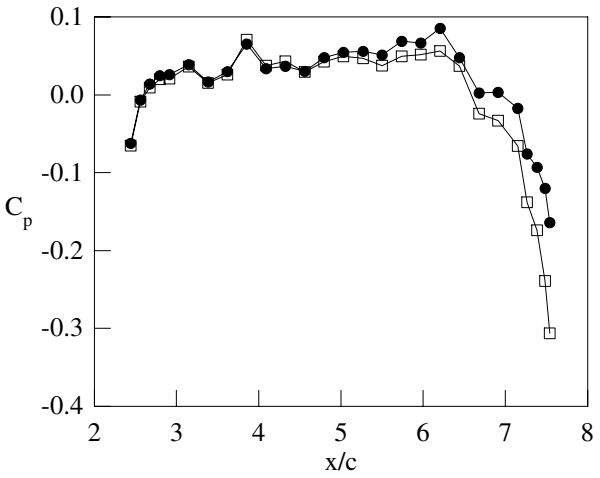

b) Ψ = 10°

Figure 36. Effect of 16-deg base flaps on trailer side centerline pressure coefficients, y/w = 0.9 (solid: baseline, open: base flaps, Re = 6 million).

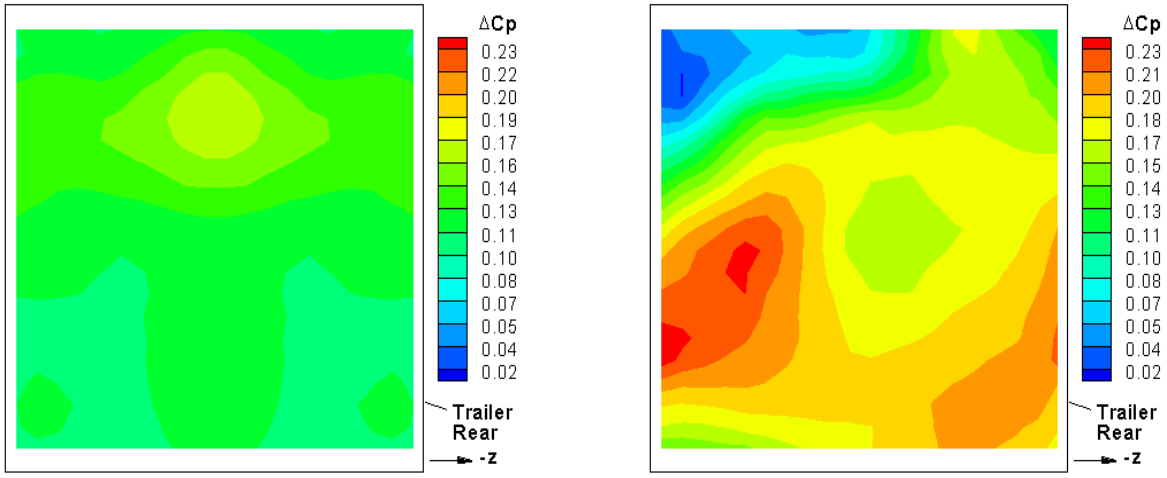

a) Ψ = 0 deg

b) Ψ = 10 deg

Figure 37. Effect of 16-deg base flaps on the pressure distribution on the back of the trailer (relative to extender baseline), Re = 6 million. Symmetry assumed for zero yaw. For Ψ = 10°, right half of image represents data at Ψ = –10°.

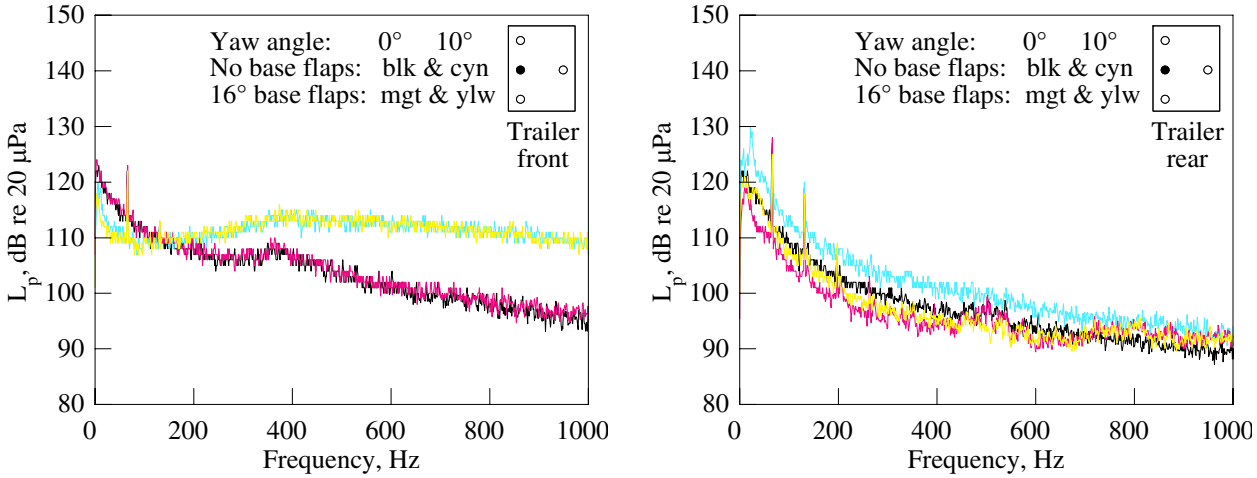

a) Trailer front

b) Trailer rear

Figure 38. Effect of trailer base flaps on dynamic pressure spectra on the rear of the trailer, Re = 6 million.

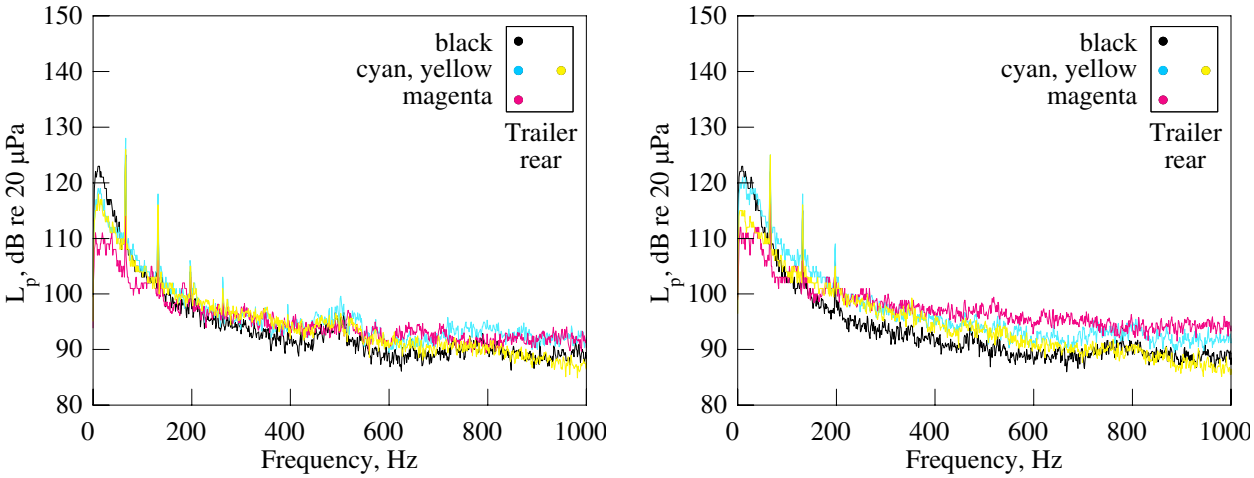

a) 0 deg

b) 10 deg

Figure 39. Effect of yaw angle and sensor position on dynamic pressure spectra with trailer base flaps, trailer rear, Re = 6 million.

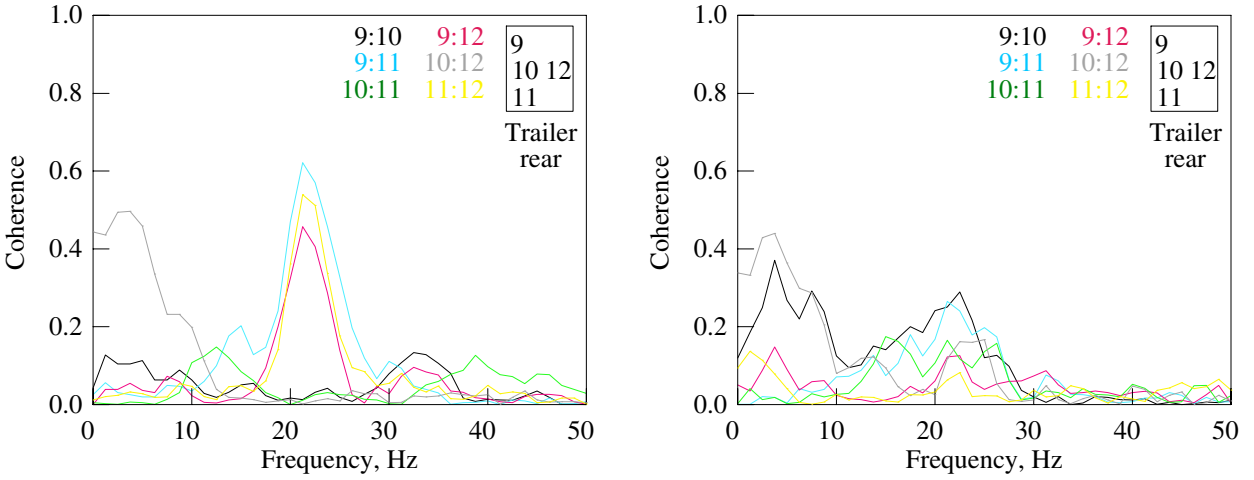

a) 0 deg

b) 10 deg

Figure 40. Dynamic-pressure signal coherence between neighboring sensors on the rear of the trailer with 60%-gap side and roof extenders, Re = 6 million.

a) Standard ($\Delta \bar{C}_D$ = –0.0582)

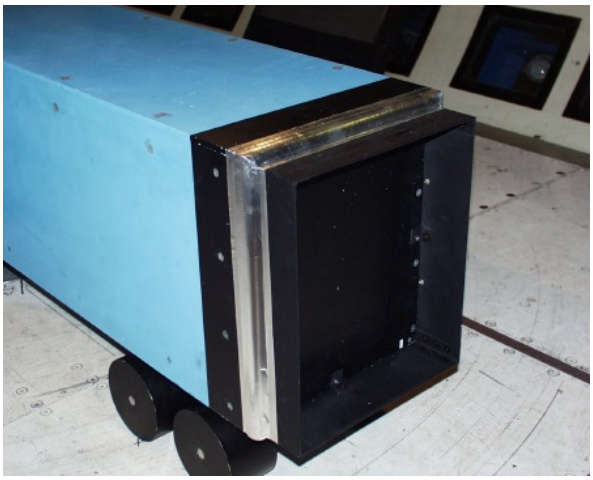

b) Shortened with fillets ($\Delta \bar{C}_D$ = –0.0573)

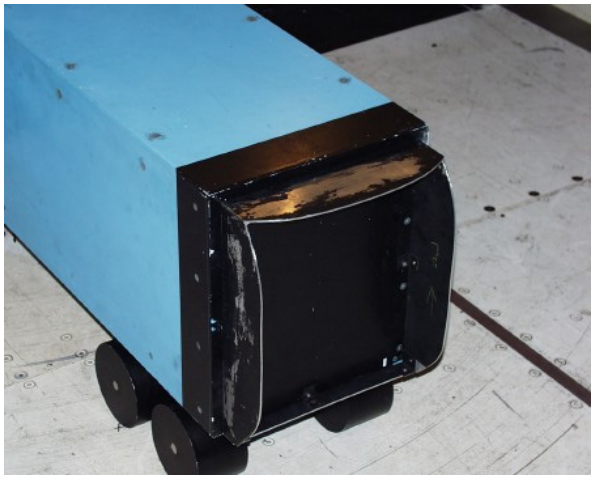

c) Scalloped ($\Delta \bar{C}_D$ = –0.0541)

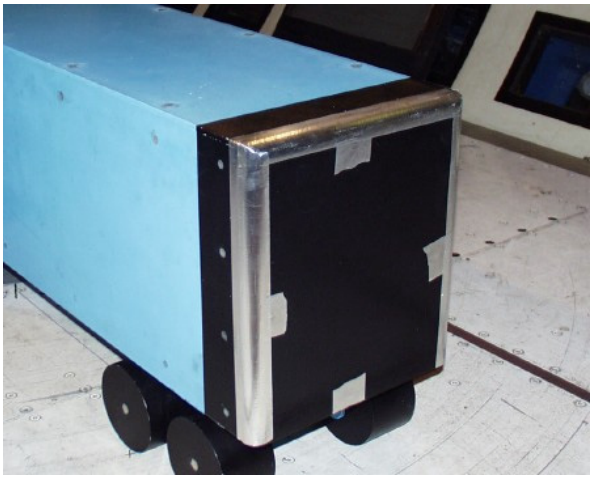

d) Rounded base plate ($\Delta \bar{C}_D$ = –0.0160)

Figure 41. Aerodynamic boattail plates and base plate installed on the base of the trailer. Change in wind-averaged drag relative to 60%-gap side and roof extenders (config. 8).

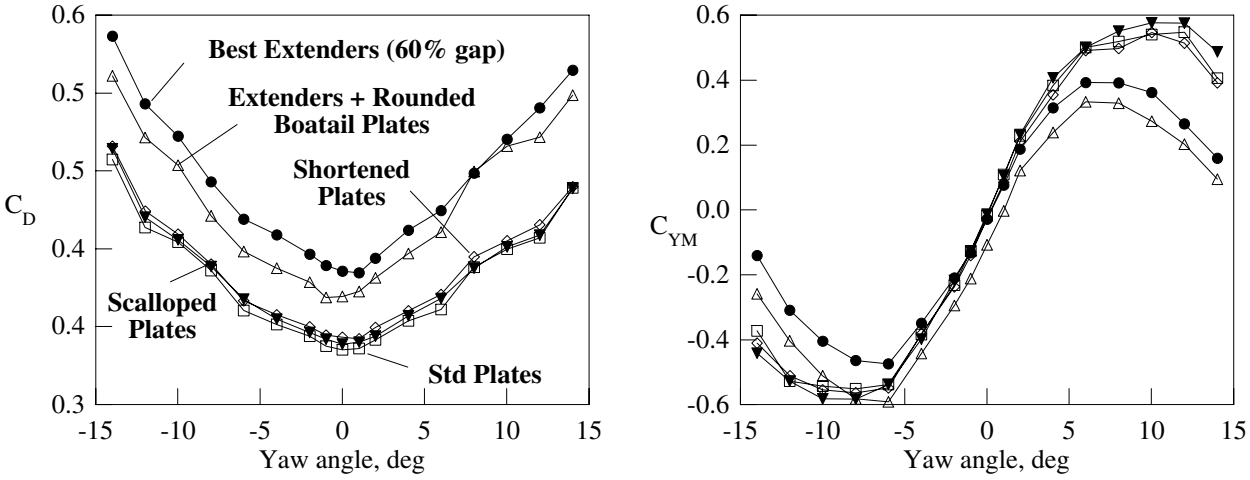

a) Drag coefficient

b) Yawing-moment coefficient

Figure 42. Effect of trailer boattail plates on body-axis drag and yawing moment coefficients. Unless otherwise specified, data are from 12-Foot Wind Tunnel at Re = 6 million.

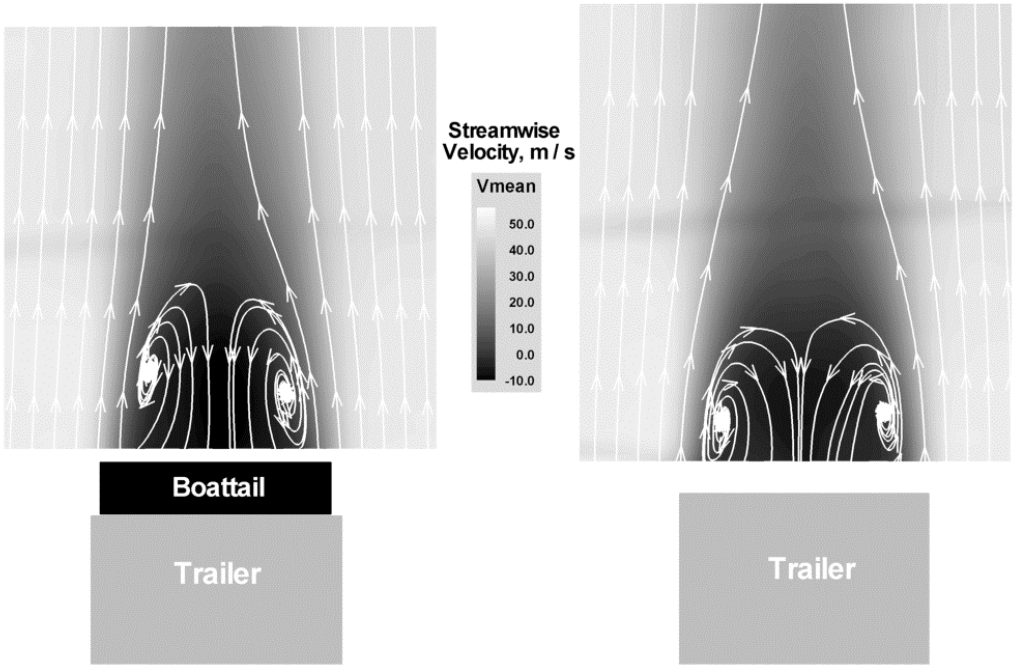

Figure 43. Particle Image Velocimetry data in the trailer wake with and without boattail plates at trailer mid-height. Images are colored by out-of-plane velocity and flow is from bottom to top (7x10-Foot Wind Tunnel, Re = 1 million).

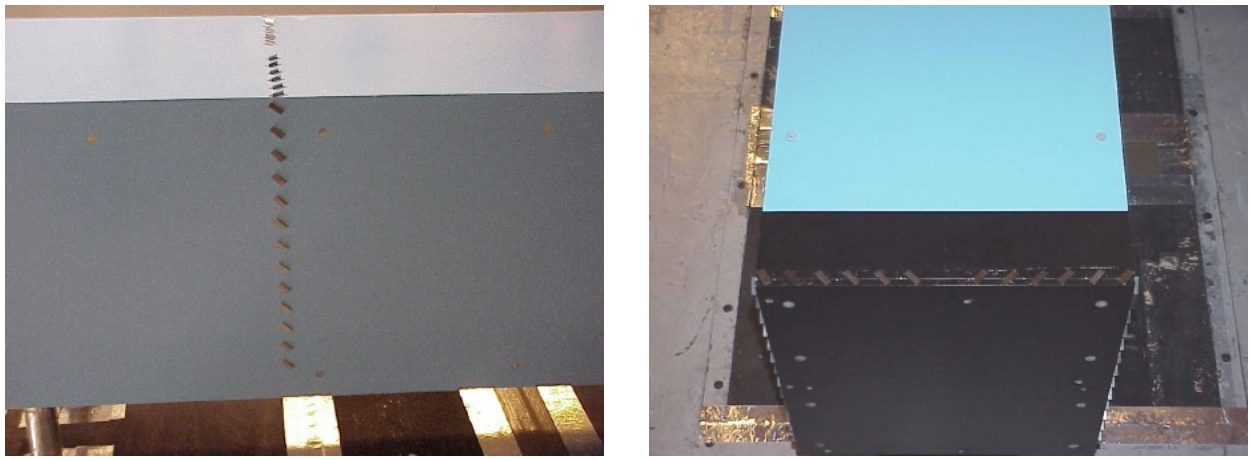

a) Mid-trailer ($\Delta \bar{C}_D = +0.0460$)

b) Rear of trailer ($\Delta \bar{C}_D = +0.0620$)

Figure 44. Vane-type vortex generators on the trailer. Change in wind-averaged drag relative to 60%-gap side and roof extenders (config. 8).

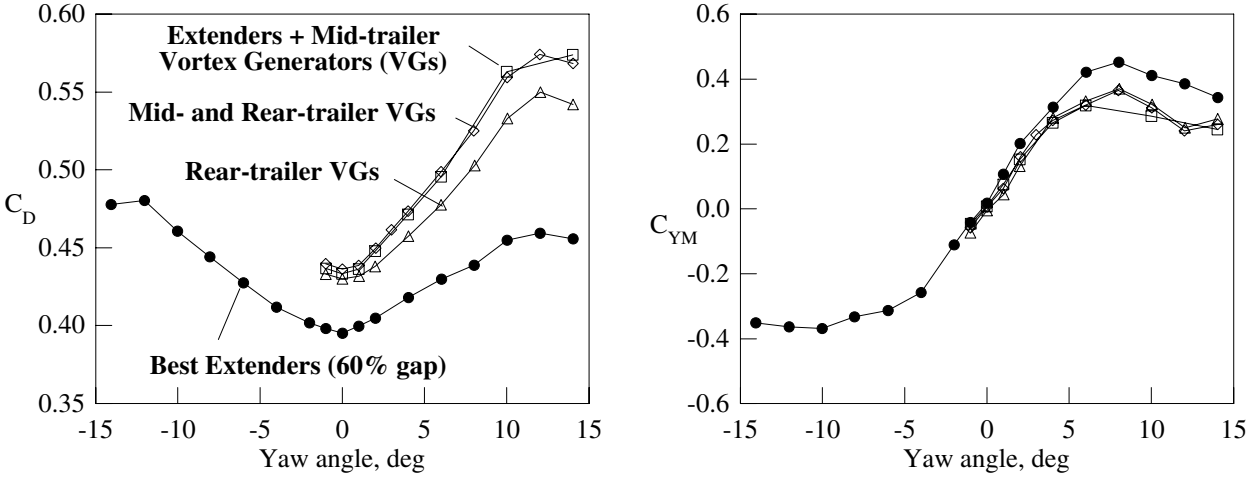

a) Drag coefficient

b) Yawing-moment coefficient

Figure 45. Effect of trailer vortex generators on body-axis drag and yawing moment coefficients. All data are from 7- by 10-Foot Wind Tunnel at Re = 1 million.

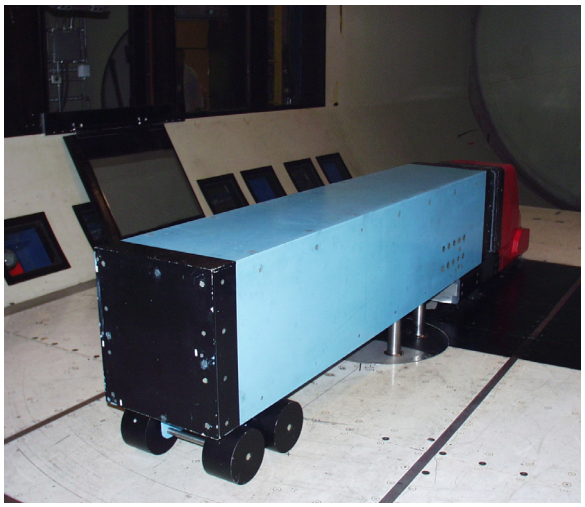

a) Side & roof extenders (baseline)

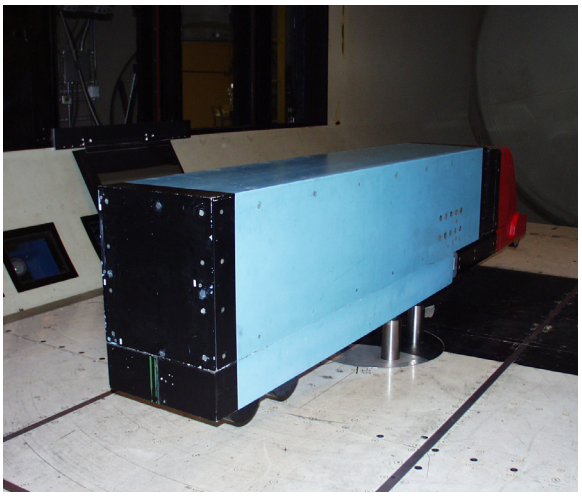

b) Trailer with belly box ($\Delta \bar{C}_D = -0.0494$)

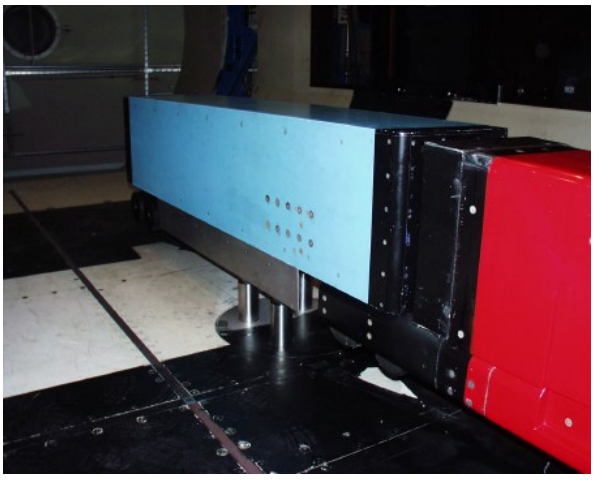

c) Side skirts ($\Delta \bar{C}_D = -0.0359$)

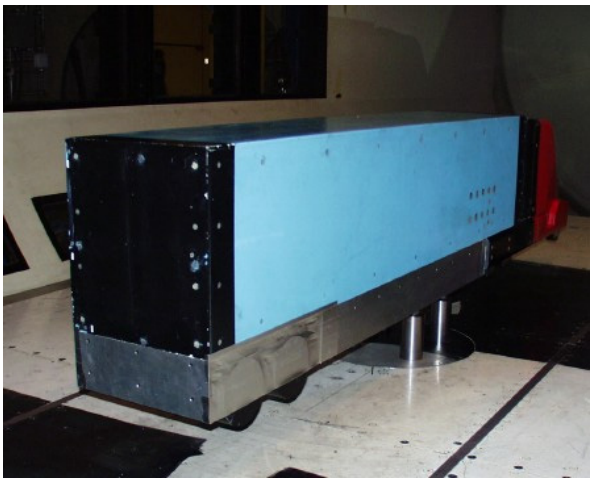

d) Full skirts ($\Delta \bar{C}_D = +0.0068$)

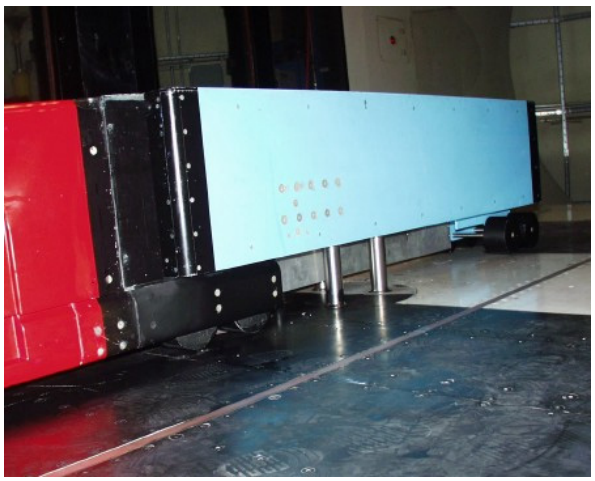

e) Centerline splitter ($\Delta \bar{C}_D = -0.0044$)

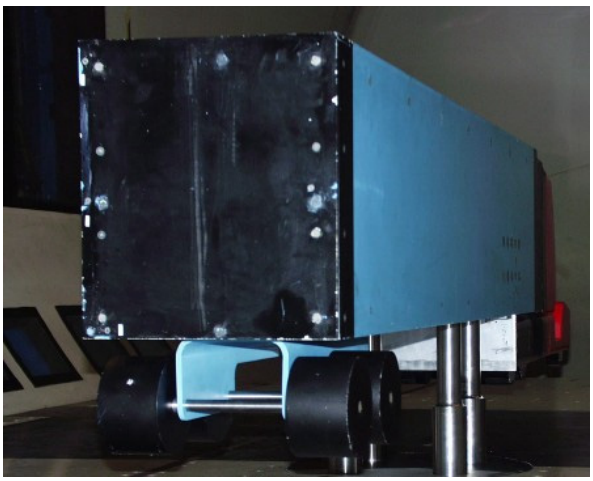

f) Cross splitter ($\Delta \bar{C}_D = +0.0356$)

Figure 46. Trailer underbody devices: belly box, skirts, and splitter plates. Change in wind-averaged drag relative to 60%-gap side and roof extenders (config. 8).

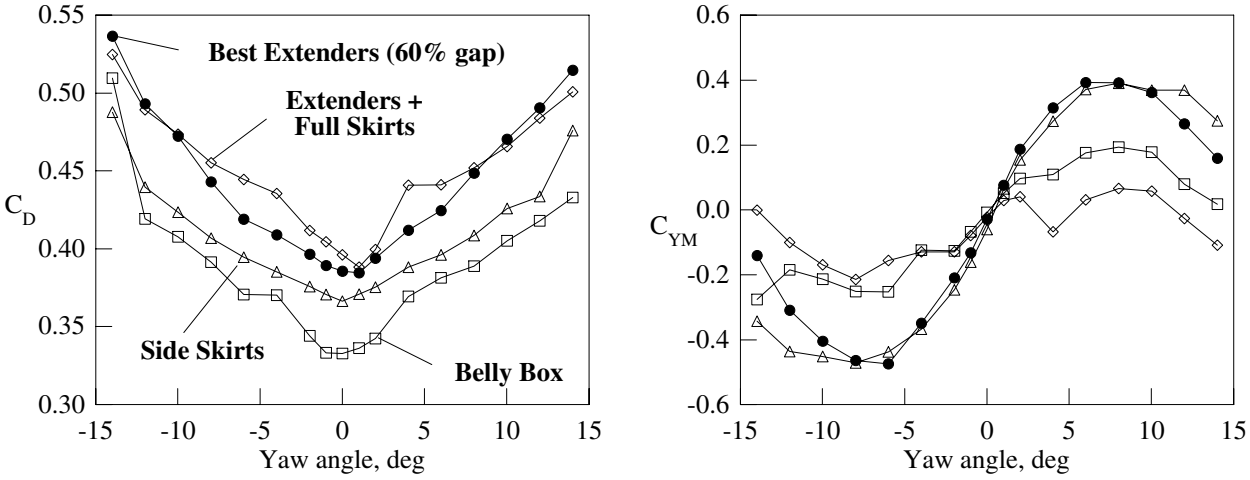

a) Drag coefficient

b) Yawing-moment coefficient

Figure 47. Effect of trailer belly box and skirts on body-axis drag and yawing moment coefficients. Unless otherwise specified, data are from 12-Foot Wind Tunnel at Re = 6 million.

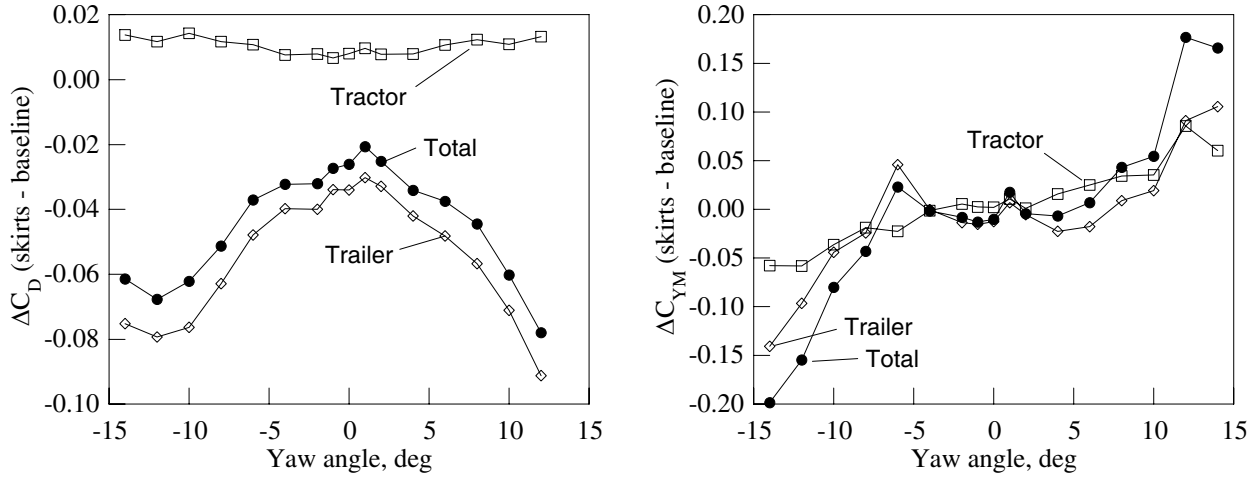

Figure 48. Effect of trailer skirts on component drag and yawing-moment differences relative to best extender baseline (config. 8) at Re = 6 million.

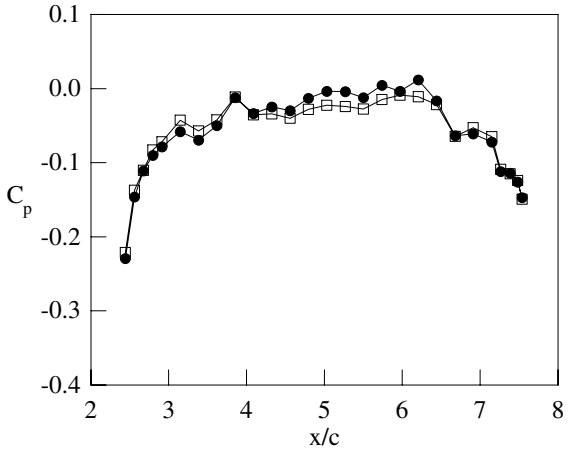

a) Ψ = 0°

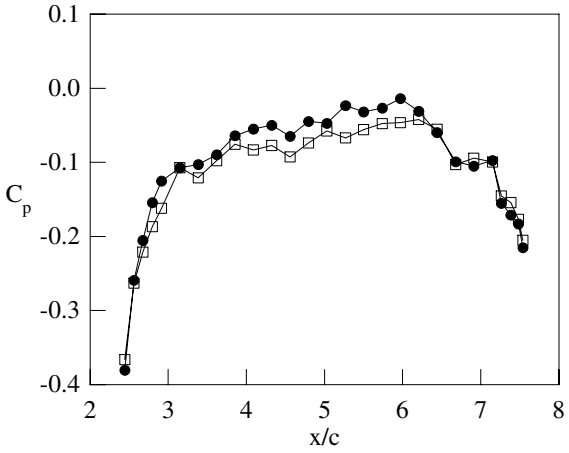

b) Ψ = 10°

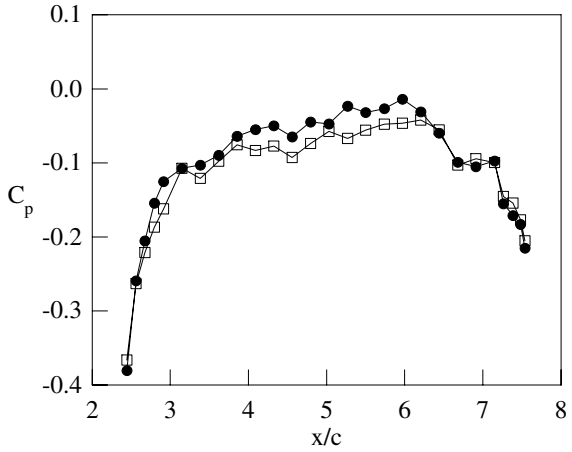

c) Ψ = 10°

Figure 49. Effect of trailer skirts on side centerline pressure coefficients, y/w = 0.9 (solid: baseline, open: skirts, Re = 6E06)

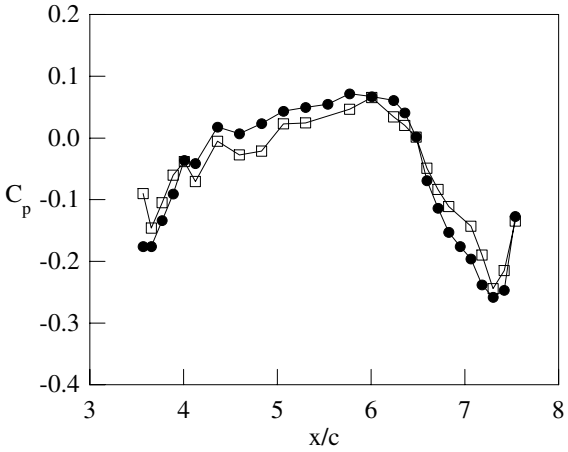

a) Ψ = 0°

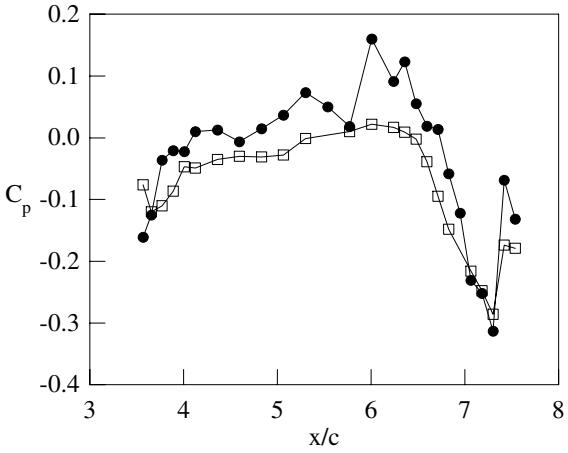

a) Ψ = 10°

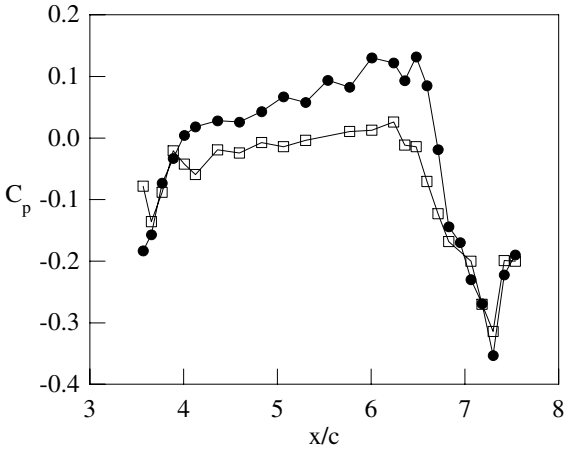

c) Ψ = 10°

Figure 50. Effect of trailer skirts on underbody pressure coefficients, z/w = 0.0 (solid: baseline, open: skirts, Re = 6E06).

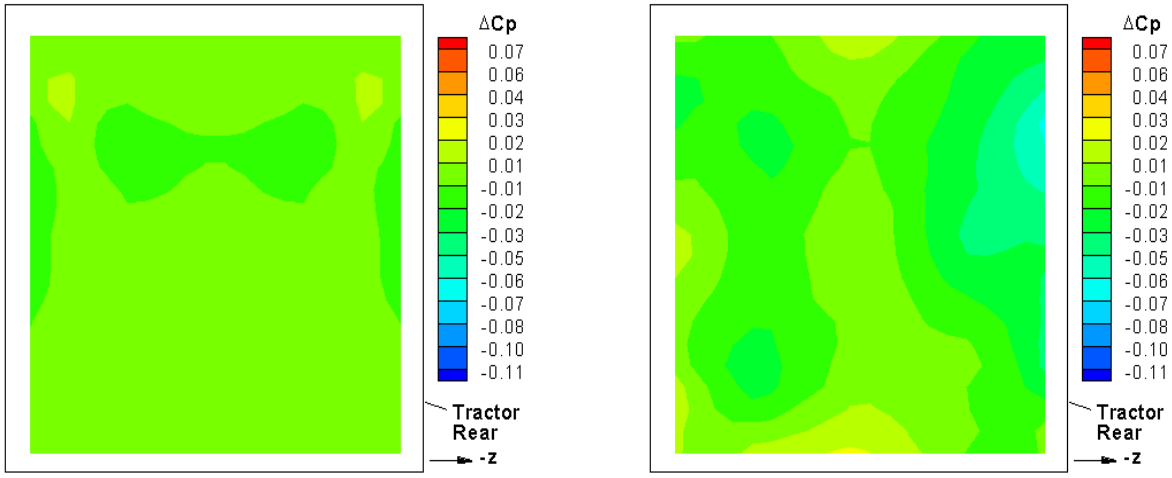

a) Ψ = 0 deg b) Ψ = 10 deg

Figure 51. Effect of trailer skirts on the pressure distribution on the back of the tractor (relative to extender baseline), Re = 6 million. Symmetry assumed for zero yaw. For Ψ = 10°, right half of image represents data at Ψ = –10°.

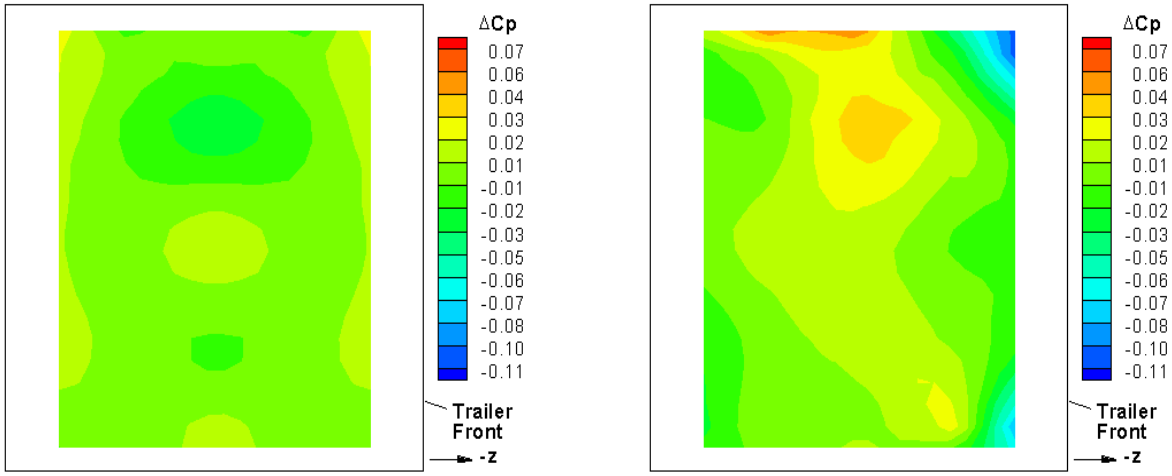

a) Ψ = 0 deg b) Ψ = 10 deg

Figure 52. Effect of trailer skirts on the pressure distribution on the front of the trailer (relative to extender baseline).

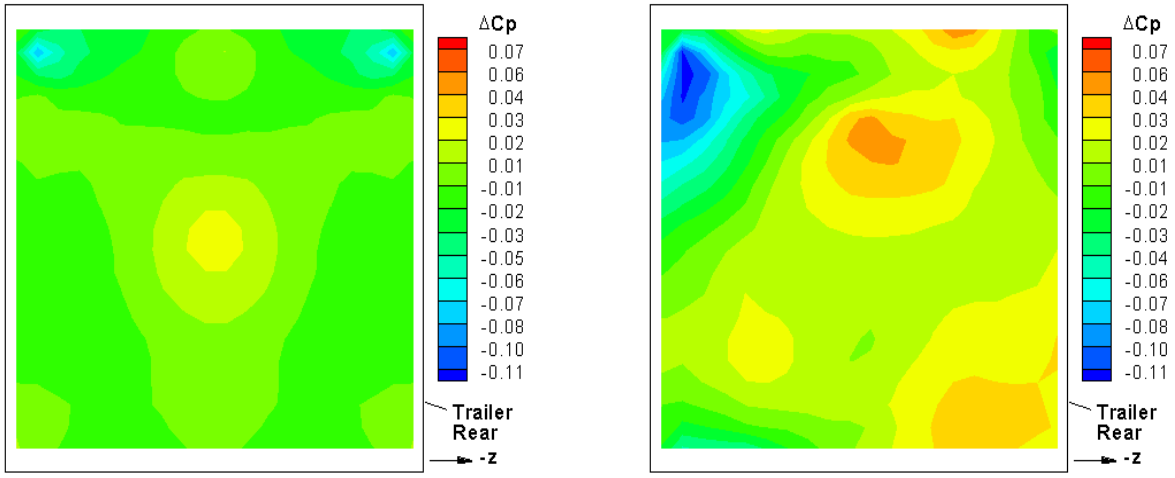

a) Ψ = 0 deg

b) Ψ = 10 deg

Figure 53. Effect of trailer skirts on the pressure distribution on the back of the trailer (relative to extender baseline).

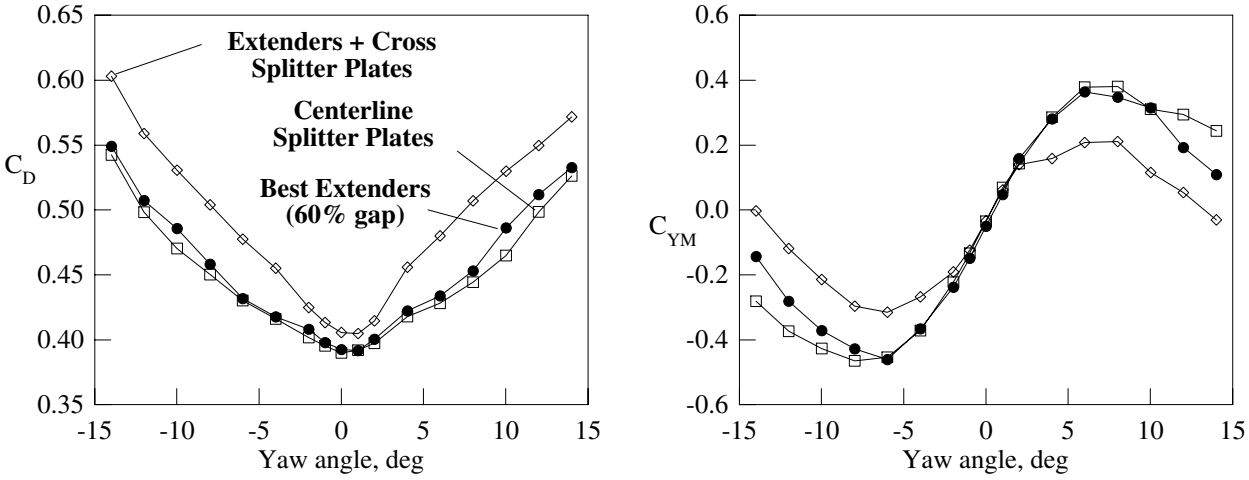

a) Drag coefficient

b) Yawing-moment coefficient

Figure 54. Effect of trailer splitter plates on body-axis drag and yawing moment coefficients (Re = 6 million, relative to config. 8, run 242).

a) GTS model (ref. 5) ($\bar{C}_D$ = 0.2770)

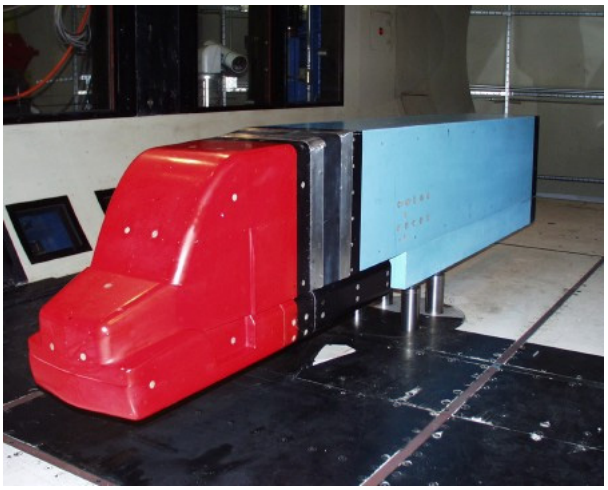

b) GCM equivalent ($\bar{C}_D$ = 0.3136)

Figure 55. Simplified models with no wheels or tractor-trailer gap.

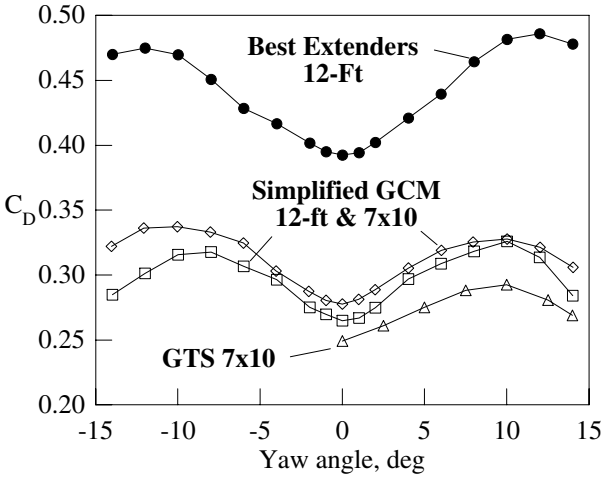

a) Drag coefficient

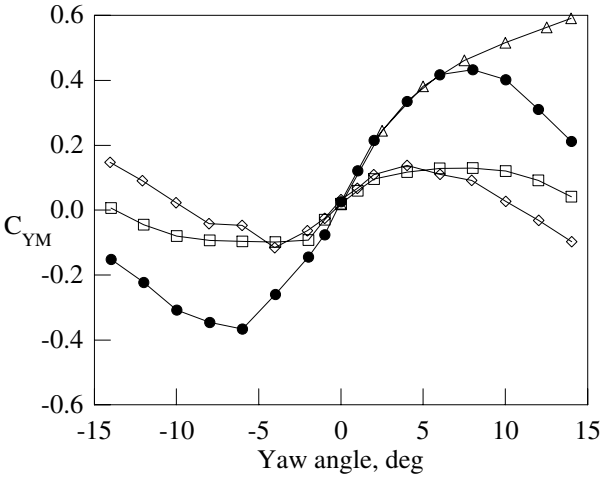

b) Yawing-moment coefficient

Figure 56. Comparison of body-axis drag and yawing moment coefficients for simplified tractor-trailer models (Re = 1 million).

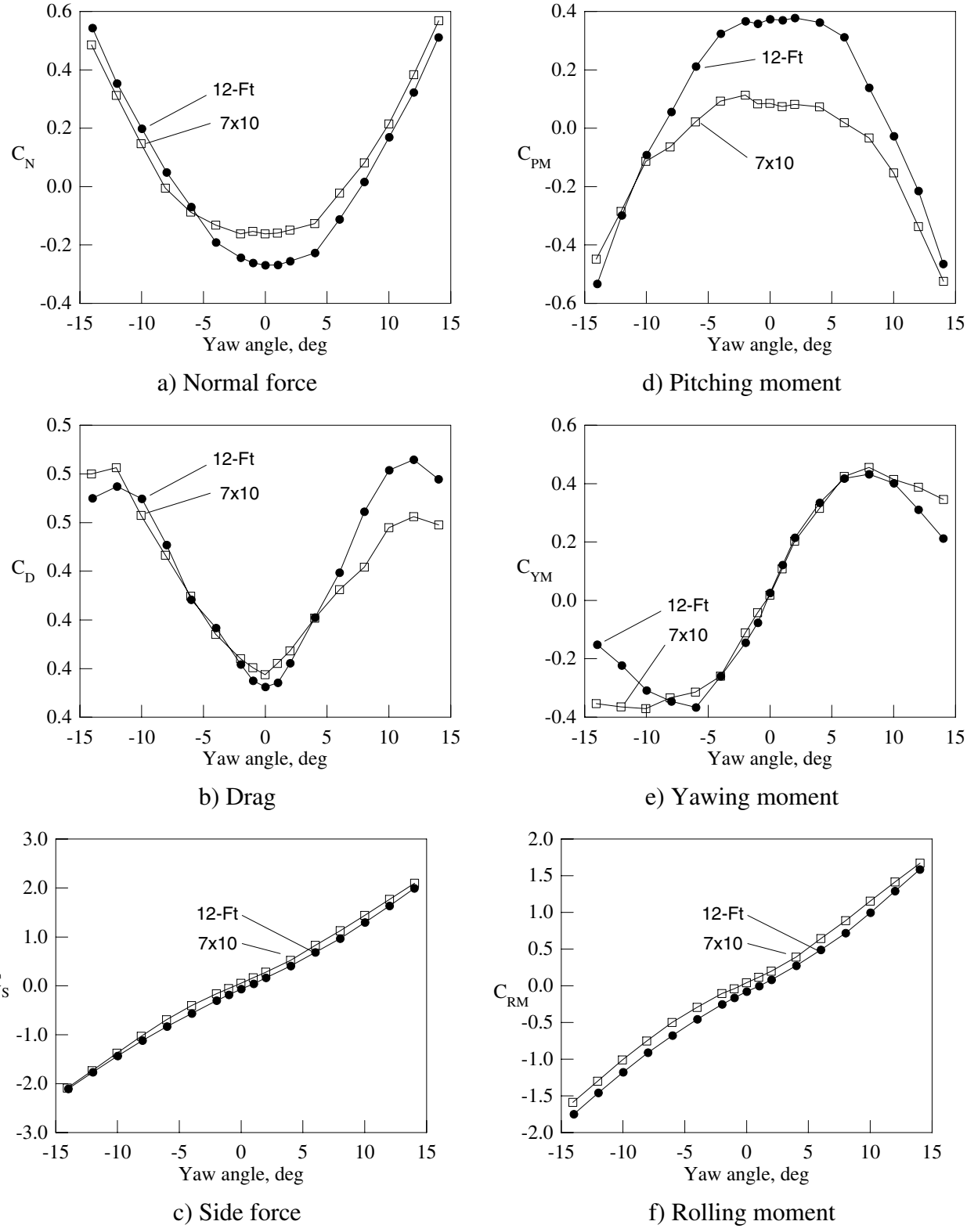

Figure 57. Comparison of the force and moment coefficients for the 60%-gap side and roof extenders (config. 8) in the 7- by 10-Foot and 12-Foot Wind Tunnels (Re = 1 million).

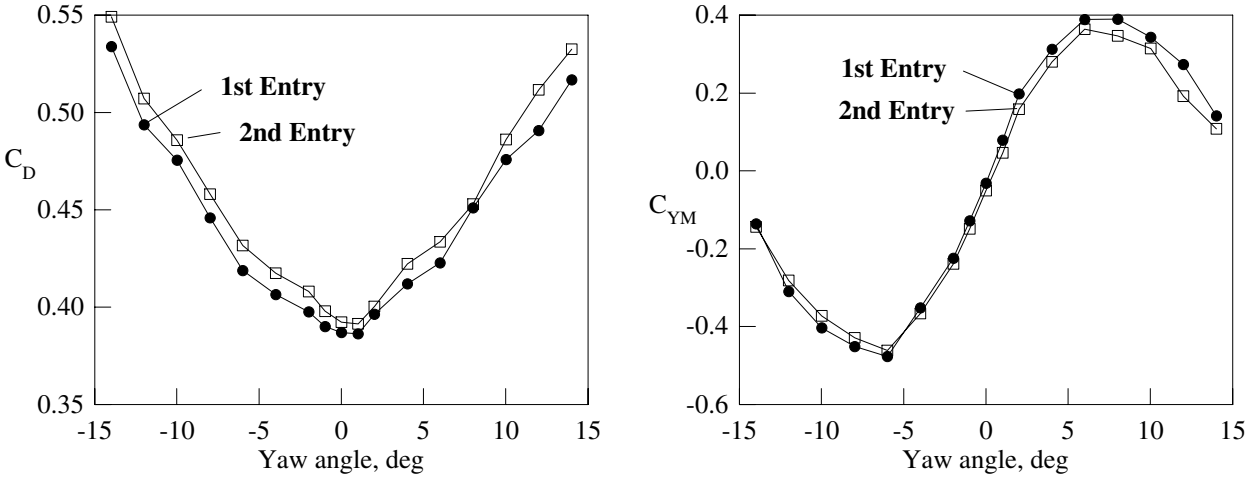

a) Drag coefficient

b) Yawing-moment coefficient

Figure 58. Comparison of body-axis drag and yawing moment coefficients for the 1st and 2nd entries in the 12-Foot Wind Tunnel (config. 8, Re = 6 million).

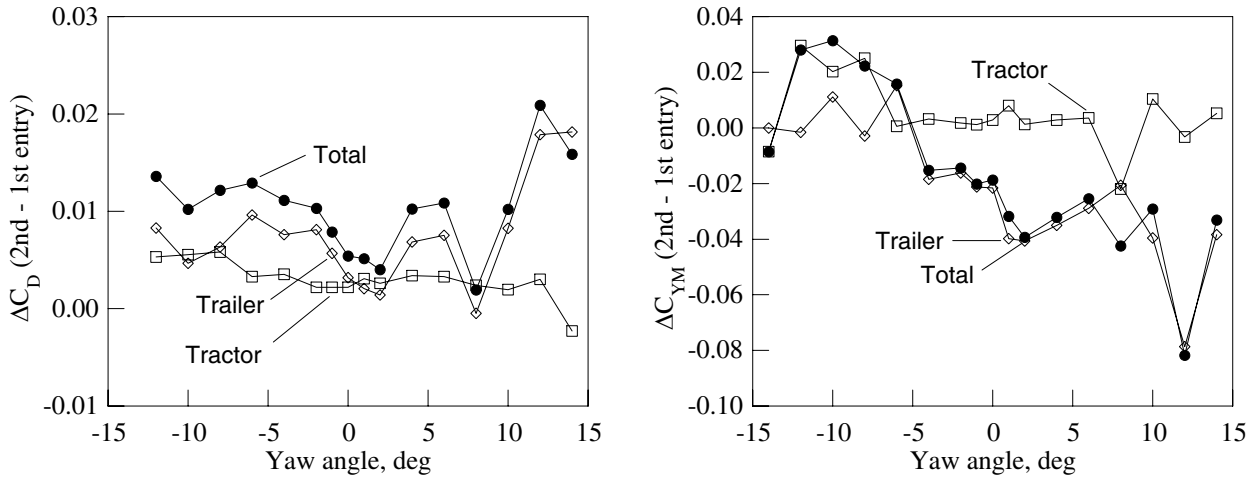

Figure 59. Comparison of component drag and yawing-moment changes between the 1st and 2nd entries in the 12-Foot Wind Tunnel (config. 8, Re = 6 million).

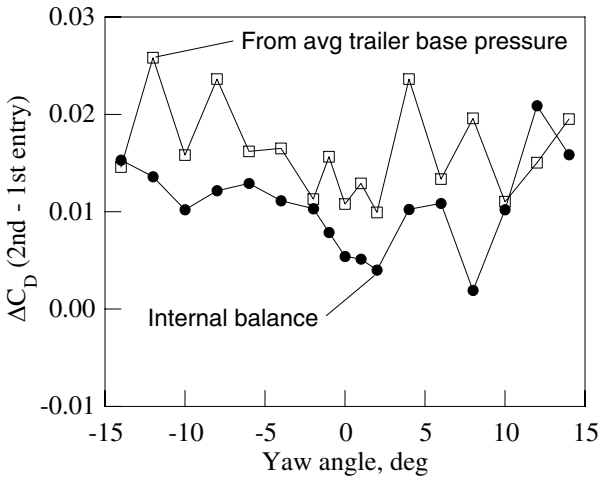

Figure 60. Comparison of drag coefficient from internal balance and average base pressure for the 1st and 2nd entries in the 12-Foot Wind Tunnel (config. 8, Re = 6 million).

APPENDIX A. GCM CONFIGURATION LIST

No.	Configuration Reynolds Number (million) =	7x10 1.1	12-Ft 1.1	2.1	3.2	4.2	5.2	6.2
1	No cab extenders	x	x	x	x	x	x	x
2	1.5" Side Extenders	x						
3	1.5" Side & Roof Extenders	x	x			x		x
4	2.0" Side & Roof Extenders	x	x	x		x		x
4.3	2.0" Side & 2.5" Roof Extenders	x						
5	2.0" Side Extenders	x						
6	2.5" Side Extenders	x						x
7	2.5" Side & Roof Extenders (Best in 7x10)	x	x		x	x		x
7.1	2.5" Extenders (tractor wheels to outside)	x						
8	3.0" Side & Roof Extenders (Best in 12-Ft)	x	x	x	x	x	x	x
9	3.0" Side Extenders	x				x		
11	No Wheels + Best Extenders	x						
11.1	No Wheels + Best Ext. - Rear strut fairings	x						
11.2	No Tractor Wheels + Best Extenders	x						
13	Best Extenders (7x10 ≠ 12-Ft) + Boattail	x	x	x	x	x	x	x
14	Boattail	x						
18	Belly Box + Best Extenders	x						x
21	Belly Box + Boattail + Best Extenders	x						
24	10" gap	x						
25	10" gap + Best Extenders	x						
26	Gap filler	x						
27	GTS = No Wheels + gap filler + Belly Box	x	x			x		x
28	1.5" Side Ext. + VGs at trailer rear	x						
28.1	1.5" Side Ext. + VGs at mid trailer & rear	x						
28.2	1.5" Side Ext. + VGs at mid trailer	x						
28.3	1.5" Side Ext. + small VGs at trailer rear	x						
29.1	Best Extenders + Base flaps (0-deg)		x	x	x	x	x	x
29.2	Best Extenders + Base flaps (4-deg)							x
29.3	Best Extenders + Base flaps (8-deg)							x
29.4	Best Extenders + Base flaps (12-deg)						x	x
29.5	Best Extenders + Base flaps (16-deg)						x	x
29.6	Best Extenders + Base flaps (20-deg)						x	
29.7	Best Extenders + Base flaps (24-deg)						x	
29.8	Best Extenders + Base flaps (28-deg)						x	
30	Best Extenders + Shortened Boattail							x
31	Best Ext. + Short Boattail + Fillets							x
32	Best Extenders + Rounded Base Plate							x
33	Best Extenders + Scalloped Boattail							x
34	Trailer Alone		x			x		x
35	Cab Splitter							x
36	Best Extenders + Trailer Centerline Splitter							x
37	Best Extenders + Trailer Cross Splitter							x
38	Best Extenders + Trailer Skirt							x
39	Best Extenders + Trailer Side Skirts							x

APPENDIX B. WIND-AVERAGED DRAG BY CONFIGURATION (BE = BEST EXTENDERS)

		7x10, Re = 1.1 million			12-Ft, Re = 1.1 million			12-Ft, Re = 6.2 million		
No.	Configuration	Run	Cdbar	ΔCdbar	Run	Cdbar	ΔCdbar	Run	Cdbar	ΔCdbar
1	No cab extenders	43	0.5778	0.1511	58	0.5823	0.1510	32	0.5777	**0.1562**
2	1.5" Side Extenders	33	0.4433	0.0166	-	-	-	-	-	-
3	1.5" Side & Roof Ext.	34	0.4349	0.0082	69	0.4344	0.0031	67	0.4330	**0.0115**
4	2.0" Side & Roof Ext.	35	0.4306	0.0039	73	0.4289	-0.0024	70	0.4285	**0.0070**
4.3	2.0" Side & 2.5" Roof	42	0.4298	0.0031	-	-	-	-	-	-
5	2.0" Side Extenders	36	0.4417	0.0150	-	-	-	-	-	-
6	2.5" Side Extenders	38	0.4339	0.0072	-	-	-	125	0.4428	**0.0213**
7	2.5" Side & Roof Ext.	39	0.4257	-0.0010	77	0.4270	-0.0043	74	0.4252	**0.0037**
7.1	2.5" Ext. (wheels out)	**58**	**0.4250**	-0.0017	-	-	-	-	-	-
8	3.0" Side & Roof Ext.	40	0.4267	0.0000	84	0.4313	0.0000	**79**	**0.4215**	**0.0000**
9	3.0" Side Extenders	41	0.4352	0.0085	-	-	-	-	-	-
11	No wheels + BE	50	0.2945	-0.1322	-	-	-	-	-	-
11.1	No wheels + BE - fairing	53	0.3182	-0.1085	-	-	-	-	-	-
11.2	No Trctr Wheels + BE	57	0.4175	-0.0092	-	-	-	-	-	-
13	BE + Boattail	**49**	**0.3757**	-0.0510	108	0.3577	-0.0736	**106**	**0.3633**	**-0.0582**
14	Boattail	78	0.5080	0.0813	-	-	-	-	-	-
18	Belly Box + BE	**61**	**0.3785**	-0.0482	-	-	-	**145**	**0.3721**	**-0.0494**
21	B. Box + Boattail + BE	**63**	**0.3075**	-0.1192	-	-	-	-	-	-
24	10" gap	68	0.5709	0.1442	-	-	-	-	-	-
25	10" gap + BE	66	0.4834	0.0567	-	-	-	-	-	-
26	Gap filler	70	0.4272	0.0005	-	-	-	-	-	-
27	GTS Config.	72	0.3136	-0.1131	151	0.3014	-0.1299	147	0.2929	**-0.1286**
28	1.5" Ext. + VGs rear	27	0.4887	0.0620	-	-	-	-	-	-
28.1	1.5" Ext. + VGs mid/rear	28	0.4902	0.0635	-	-	-	-	-	-
28.2	1.5" Ext. + VGs mid	29	0.4727	0.0460	-	-	-	-	-	-
28.3	1.5" Ext + small VGs	30	0.4816	0.0549	-	-	-	-	-	-
29.1	BE + Base flaps (0-deg)	-	-	-	-	-	-	126	0.4025	**-0.0190**
29.2	BE + Base flaps (4-deg)	-	-	-	-	-	-	127	0.3950	**-0.0265**
29.3	BE + Base flaps (8-deg)	-	-	-	-	-	-	128	0.3815	**-0.0400**
29.4	BE + Base flaps (12-deg)	-	-	-	-	-	-	129	0.3742	**-0.0473**
29.5	BE + Base flaps (16-deg)	-	-	-	-	-	-	131	0.3429	**-0.0786**
29.6	BE + B. flaps (20-deg) *	-	-	-	-	-	-	241	0.3360	-0.0954
29.7	BE + B. flaps (24-deg) *	-	-	-	-	-	-	237	0.3467	-0.0847
29.8	BE + B. flaps (28-deg) *	-	-	-	-	-	-	238	0.4171	-0.0143
30	BE + Shortened Boattail	-	-	-	-	-	-	109	0.3703	-0.0512
31	BE + Short w/ fillets	-	-	-	-	-	-	110	0.3642	-0.0573
32	BE + Rounded Base	-	-	-	-	-	-	111	0.4055	-0.0160
33	BE + Scalloped Boattail	-	-	-	-	-	-	113	0.3674	-0.0541
34	Trailer Alone	-	-	-	158	0.6509	0.2196	154	0.6637	0.2422
35	Cab Splitter *	-	-	-	-	-	-	247	0.4815	0.0501
36	BE + Centerline Splitter *	-	-	-	-	-	-	243	0.4270	-0.0044
37	BE + Cross Splitter *	-	-	-	-	-	-	244	0.4670	0.0356
38	BE + Trailer Skirt *	-	-	-	-	-	-	245	0.4382	0.0068
39	BE + Trailer Side Skirts *	-	-	-	-	-	-	248	0.3955	-0.0359

* ΔCdbar relative to 2nd entry baseline (config. 8, Run 242). All others relative to row no. 8.

REPORT DOCUMENTATION PAGE

Form Approved
OMB No. 0704-0188

1. REPORT DATE *(DD-MM-YYYY)*	2. REPORT TYPE	3. DATES COVERED *(From - To)*
28-07-2006	Technical Memorandum	

4. TITLE AND SUBTITLE

A Summary of the Experimental Results for a Generic Tractor-Trailer in the Ames Research Center 7- by 10-Foot and 12-Foot Wind Tunnels

5a. CONTRACT NUMBER

5b. GRANT NUMBER

5c. PROGRAM ELEMENT NUMBER

6. AUTHOR(S)

Bruce L. Storms[1], Dale R. Satran[2], James T. Heineck[2], and Stephen M. Walker[2]

5d. PROJECT NUMBER

5e. TASK NUMBER

5f. WORK UNIT NUMBER

522-21-72-52-98

7. PERFORMING ORGANIZATION NAME(S) AND ADDRESS(ES)

[1]Aerospace Computing, Inc. , Ames Research Center
Moffett Field, CA 94035-1000 and
[2]Ames Research Center, Moffett Field, CA 94035-1000

8. PERFORMING ORGANIZATION REPORT NUMBER

A-060009

9. SPONSORING/MONITORING AGENCY NAME(S) AND ADDRESS(ES)

National Aeronautics and Space Administration
Washington, DC 20546-0001

U.S. Department of Energy, Washington, DC 20585

10. SPONSORING/MONITOR'S ACRONYM(S)

NASA

11. SPONSORING/MONITORING REPORT NUMBER

NASA/TM–2006-213489

12. DISTRIBUTION/AVAILABILITY STATEMENT

Unclassified — Unlimited Distribution: Nonstandard
Subject Category: 02
Availability: NASA CASI (301) 621-0390

13. SUPPLEMENTARY NOTES

Point of Contact: Bruce L. Storms, Ames Research Center, M.S. 260-1, Moffett Field, CA 94035-1000
(650) 604-1356

14. ABSTRACT

Experimental measurements of a generic tractor-trailer were obtained in two wind tunnels at Ames Research Center. After a preliminary study at atmospheric conditions in the 7- by 10-Foot Wind Tunnel, additional testing was conducted at Reynolds numbers corresponding to full-scale highway speeds in the 12-Foot Pressure Wind Tunnel. To facilitate computational modeling, the 1:8-scale geometry, designated the Generic Conventional Model, included a simplified underbody and omitted many small-scale details. The measurements included overall and component forces and moments, static and dynamic surface pressures, and three-component particle image velocimetry. This summary report highlights the effects of numerous drag reduction concepts and provides details of the model installation in both wind tunnels. To provide a basis for comparison, the wind-averaged drag coefficient was tabulated for all configurations tested. Relative to the baseline configuration representative of a modern class-8 tractor-trailer, the most effective concepts were the trailer base flaps and trailer belly box providing a drag-coefficient reduction of 0.0855 and 0.0494, respectively. Trailer side skirts were less effective yielding a drag reduction of 0.0260. The database of this experimental effort is publicly available for further analysis.

15. SUBJECT TERMS

Bluff body aerodynamics, Truck drag, Underbody

16. SECURITY CLASSIFICATION OF:			17. LIMITATION OF ABSTRACT	18. NUMBER OF PAGES	19a. NAME OF RESPONSIBLE PERSON
a. REPORT	b. ABSTRACT	c. THIS PAGE			Bruce L. Storms
Unclassified	Unclassified	Unclassified	Unclassified	54	19b. TELEPHONE *(Include area code)* (650) 604-1356